



Simulated last deglaciation of the Barents Sea Ice Sheet primarily driven by oceanic conditions

Michele Petrini^{a, j, *}, Florence Colleoni^a, Nina Kirchner^{b, c}, Anna L.C. Hughes^{d, e}, Angelo Camerlenghi^a, Michele Rebesco^a, Renata G. Lucchi^{a, f}, Emanuele Forte^g, Renato R. Colucci^h, Riko Noormetsⁱ, Jan Mangerud^d

^a OGS (Istituto Nazionale di Oceanografia e Geofisica Sperimentale), Borgo Grotta Gigante 42/c, 34010, Sgonico (TS), Italy

^b Bolin Centre for Climate Research, Stockholm University, SE-106 91, Stockholm, Sweden

^c Department of Physical Geography, Stockholm University, SE-106 91, Stockholm, Sweden

^d Department of Earth Science, University of Bergen and Bjerknes Centre for Climate Research, N-5007, Bergen, Norway

^e Department of Geography, University of Manchester, Oxford Rd M13 9PL, Manchester, UK

^f Centre for Arctic Gas Hydrate (CAGE), Environment and Climate UiT, The Arctic University of Norway, Tromsø

^g Dipartimento di Matematica e Geoscienze, Università di Trieste, via Weiss 1, 34128, Trieste (TS), Italy

^h ISMAR (Istituto di Scienze Marine), Trieste, Italy

ⁱ The University Centre in Svalbard (UNIS), P.O. Box 156 Northern-9171, Longyearbyen, Norway

^j Department of Geoscience and Remote Sensing, Delft University of Technology (TUDelft), Delft, Netherlands

ARTICLE INFO

Article history:

Received 20 December 2019

Received in revised form

14 April 2020

Accepted 14 April 2020

Available online 19 May 2020

Keywords:

Quaternary

Glaciology

Barents sea

Ice sheet modelling

Ocean melting

ABSTRACT

The Barents Sea Ice Sheet was part of an interconnected complex of ice sheets, collectively referred to as the Eurasian Ice Sheet, which covered north-westernmost Europe, Russia and the Barents Sea during the Last Glacial Maximum (around 21 ky BP). Due to common geological features, the Barents Sea component of this ice complex is seen as a paleo-analogue for the present-day West Antarctic Ice Sheet. Investigating key processes driving the last deglaciation of the Barents Sea Ice Sheet represents an important tool to interpret recent observations in Antarctica over the multi-millennial temporal scale of glaciological changes. We present results from a perturbed physics ensemble of ice sheet model simulations of the last deglaciation of the Barents Sea Ice Sheet, forced with transient atmospheric and oceanic conditions derived from AOGCM simulations. The ensemble of transient simulations is evaluated against the data-based DATED-1 reconstruction to construct minimum, maximum and average deglaciation scenarios. Despite a large model/data mismatch at the western and eastern ice sheet margins, the simulated and DATED-1 deglaciation scenarios agree well on the timing of the deglaciation of the central and northern Barents Sea. We find that the simulated deglaciation of the Barents Sea Ice Sheet is primarily driven by the oceanic forcing, with prescribed eustatic sea level rise amplifying the ice sheet sensitivity to sub-shelf melting over relatively short intervals. Our results highlight that the sub-shelf melting has a very strong control on the simulated grounding-line flux, showing that a slow, gradual ocean warming trend is capable of triggering sustained grounded ice discharge over multi-millennial timescales, even without taking into account marine ice sheet or ice cliff instability.

© 2020 Elsevier Ltd. All rights reserved.

Abbreviations: LGM, Last Glacial Maximum; SIS, Scandinavian Ice Sheet; BISS, British-Irish Ice Sheet; BSIS, Barents Sea Ice Sheet; WAIS, West Antarctic Ice Sheet; MISO, Marine Ice Sheet Instability; MICI, Marine ice-cliff instability; mLHS, maximum Latin Hypercube Sampling; AOGCM, Atmosphere-Ocean General Circulation Model; SIA, Shallow Ice Approximation; SSA, Shallow Shelf Approximation.

* Corresponding author. OGS (Istituto Nazionale di Oceanografia e Geofisica Sperimentale), Borgo Grotta Gigante 42/c, 34010, Sgonico (TS), Italy.

E-mail address: M.Petrini@tudelft.nl (M. Petrini).

1. Introduction

During the Last Glacial Maximum (LGM, around 21 ky BP) an interconnected complex of ice sheets covered Northern Eurasia, forming a continuous ice cover extending from the Atlantic continental shelf south-west of Great Britain to northeast of Franz Josef Land, over the Kara Sea. This complex, collectively referred to as the Eurasian Ice sheets, comprised three large ice sheets: the Scandinavian Ice Sheet (SIS), the British-Irish Ice Sheet (BIIS) and the

Barents Sea Ice Sheet (BSIS) (Hughes et al., 2016). The former two ice sheets were predominantly terrestrial, whereas the BSIS was almost entirely marine-based (Fig. 1). As first observed by Mercer in the early 1970s (Mercer, 1970), the BSIS shares common geological features with the present-day West Antarctic Ice Sheet (WAIS). In fact, the two ice sheets have similar size, are located in high polar regions and have their base resting on a relatively soft sediments bed.

Several recent studies show that over the last decades marine-terminating glaciers and ice shelves of the WAIS are rapidly retreating (Cook et al., 2016; Rignot et al., 2013) and thinning (Paolo et al., 2015), primarily due to the intrusion of relatively warm Circumpolar Deep Water in the cavities underneath the ice-shelves and close to the grounding zone (Rignot et al., 2013; Pritchard et al., 2012; Schmidtke et al., 2014; Khazendar et al., 2016), although there is also evidence in favor of surface warming (Rebesco et al.,

2014a). However, to what extent ice-shelf thinning or collapse might trigger sustained grounded ice discharge into the ocean remains highly uncertain, precluding well-constrained future projections of the WAIS contribution to future global-mean sea level rise (Edwards et al., 2019; Colleoni et al., 2018). Both ice sheet modelling studies and observations suggest that ice-shelf thinning or collapse in West Antarctica can potentially trigger two positive feedback effects, marine ice-sheet instability (MISI (Schoof, 2012; Rignot et al., 2014; Favier et al., 2014; Joughin et al., 2014)) and marine ice-cliff instability (MICI (DeConto and Pollard, 2016; Pollard et al., 2015)), leading in turn to widespread, accelerated and sustained mass loss. However, the use of existing parametrisations to represent these feedbacks in ice sheet model simulations is still debated, as it might lead to an overestimated ice sheet response to ocean warming (Gudmundsson et al., 2012; Petrini et al., 2018; Edwards et al., 2019). Direct measurements of the dynamic

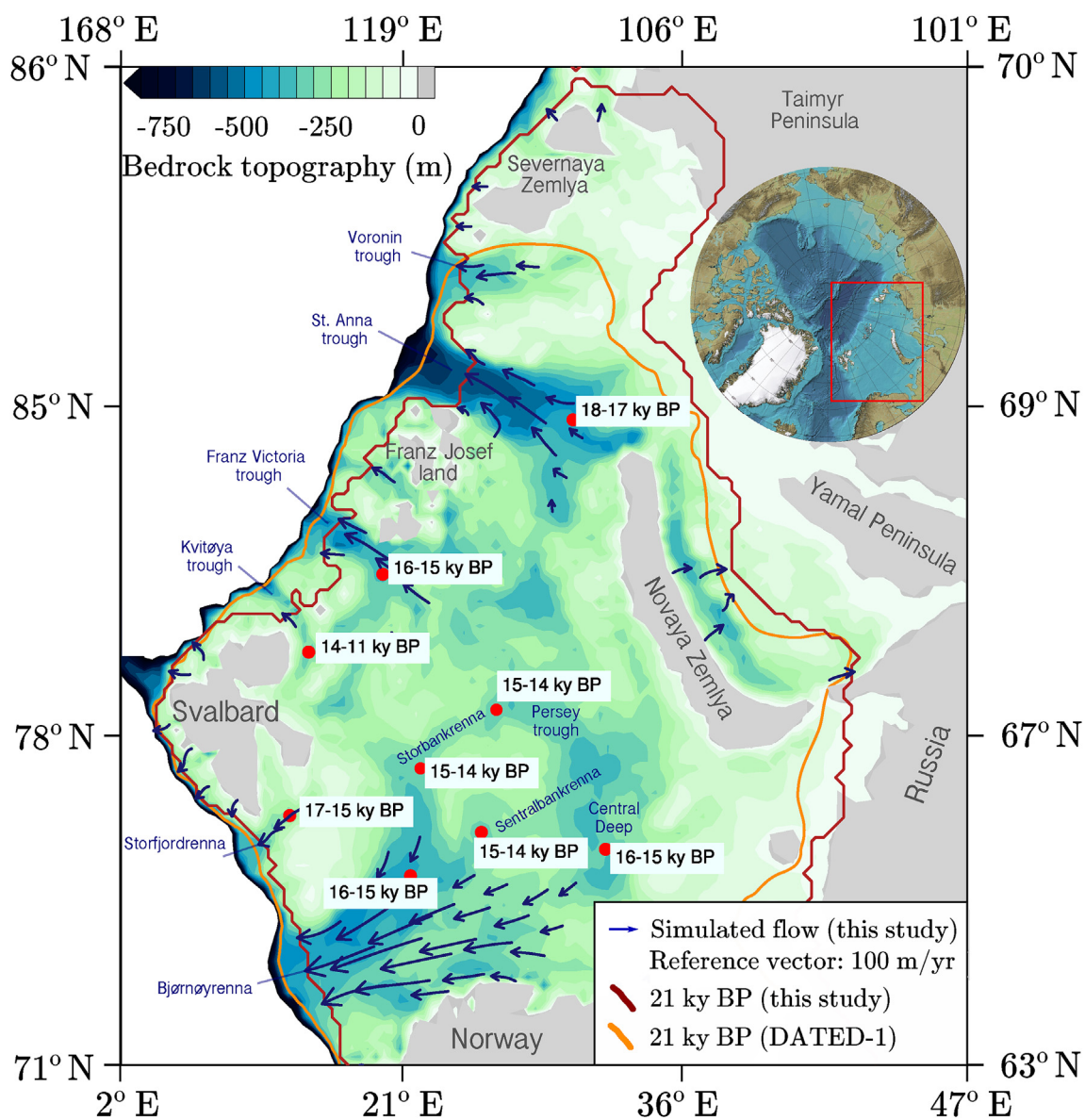


Fig. 1. Bathymetric map of the Barents and Kara seas, based on the International bathymetric chart of the Arctic Ocean (IBCAO) (Jakobsson, 2014) and interpolated in the 20 km horizontal resolution ice sheet model grid. The DATED-1 (Hughes et al., 2016) (dark yellow line) and simulated (this study, dark red line) BSIS extent during the LGM are shown. Blue arrows indicate the simulated (this study) ice velocities during the LGM (velocities lower than 45 m/yr masked out), whereas red dots indicate the location of the grid points used to estimate the individual ice streams deglaciation timing (Fig. 11). The time intervals for each location refer to its deglaciation timing range between the DATED-1 (Hughes et al., 2016) minimum and maximum reconstructions. (For interpretation of the references to color in this figure legend, the reader is referred to the Web version of this article.)

response of the WAIS to ocean warming are difficult to acquire because of the large spatio-temporal scale of glaciological changes (Colleoni et al., 2018). A valid alternative to fulfil this knowledge gap is to look at evidence of past ice sheet retreats both in the Northern and Southern Hemisphere. In this study, we focus on the last deglaciation of the BSIS. Paleo data show that after reaching its maximum extent during the LGM, the BSIS experienced a relatively rapid, stepwise retreat, leaving the Barents and Kara seas continental shelf ice-free around 14 ky BP (Hughes et al., 2016). Available marine geophysical data provide insights on the ice sheet dynamics and retreat patterns throughout the deglaciation. Therefore, the last deglaciation of the BSIS represents an excellent testing ground to validate the ability of ice sheet models to reproduce fast transitions, in order to better constrain the evolution of the WAIS in response to global warming.

In this study, we present results from a perturbed physics ensemble of 100 transient simulations of the BSIS during the last deglaciation. The simulations are performed with the GRISLI Ice Shelf and Land Ice model (GRISLI (Ritz et al., 2001)), a zero-order hybrid model (Kirchner et al., 2011) which is able to simulate ice sheet/stream/shelf systems. In order to evaluate the response of the marine-based BSIS to ice shelf thinning resulting from ice-ocean interactions, we explicitly compute sub-shelf melting by means of a two-equations formulation, based on a quadratic, local dependency of melting rates on the ocean thermal forcing (Holland et al., 2008). This formulation, similar to that used in the ice sheet model simulations contributing to the ISMIP6 projections for the Antarctic Ice Sheet (Barthel et al., 2019; Seroussi et al., 2019), has shown a good agreement with coupled ocean-ice sheet simulations under idealised future ocean warming scenarios (Favier et al., 2019).

In order to prevent possible biases in increased sub-shelf melting rates due to the ice physics response, GRISLI does not include any of the existing parametrisations for MISI and MICI feedbacks (Gudmundsson et al., 2012; Petrini et al., 2018; Edwards et al., 2019). To reduce uncertainties due to poorly constrained ice sheet model parameters, we perform a maxi-min Latin Hypercube Sampling (mLHS) of five parameters, related to the surface elevation feedback, ice dynamics and sensitivity to ocean warming. An ensemble of 100 transient simulations is performed, each run with a different combination of the selected model parameters. This perturbed physics ensemble of simulations is first tested against the data-based deglacial chronologies from the DATED-1 archive (Hughes et al., 2016). We select a group of simulations in the ensemble satisfying minimal requirements of ice sheet extent model-data agreement, and we use this group of simulations to construct minimum, maximum and average deglaciation scenarios. These three scenarios are then analyzed and compared with the DATED-1 deglacial chronologies.

2. Glacial history of the Barents and Kara seas

The Barents and Kara seas' continental shelf is characterised by a relatively uneven bathymetry, alternating shallow banks (100–200 m deep), deep transverse troughs (300–500 m deep) and several archipelagos (Svalbard, Franz Josef Land, Novaya Zemlya and Severnaya Zemlya, Fig. 1). Geological records suggest that this region was repeatedly glaciated during the late Cenozoic (Vorren et al., 1988), with several major glacial advances, from which two glacial maxima (140 ky BP and 21 ky BP) occurring in the last 160 kyrs (Svendsen et al., 2004). The LGM occurred during the Late Weichselian (Svendsen et al., 2004; Landvik et al., 1998) between 25 and 23 ky BP, when ice masses over Svalbard, Novaya Zemlya and Franz Josef Land coalesced into an integrated BSIS (Hughes et al., 2016).

Sediment cores from trough-mouth fans and offshore ice rafted debris suggest that the western and northern margins of the BSIS extended up or close to the continental shelf edge during the LGM (Landvik et al., 1998; Andersen et al., 1996; Kleiber et al., 2000). Subsequent studies analyzing data from the south-western, central and northern Barents Sea confirmed this reconstruction (Fig. 1). In contrast, the extent of the eastern margin of the ice sheet during the LGM has been debated since the late 1990s (Svendsen et al., 2004). The data-based reconstruction DATED-1 (Hughes et al., 2016) suggests that the ice sheet extended over Novaya Zemlya in the eastern Kara Sea, but never reached the mainland Russia and Siberia (Fig. 1), with the exception of a short-lived advance of an ice lobe over the north-western Taymyr Peninsula slightly prior than the LGM (Hughes et al., 2016). This is in contradiction with previously published reconstructions based on glacial isostatic adjustment modelling (Peltier, 2004; Peltier et al., 2015), claiming that the ice sheet extent over north-western Taymyr in the north-east was sustained during the LGM. In the south, there is no doubt that the BSIS and the SIS were connected at the LGM, although the timing of coalescence of these two ice sheets is not well constrained due to a lack of chronological data (Hughes et al., 2016).

Marine geophysical data from the Barents Sea continental shelf and slope show that during the LGM the BSIS was drained by several ice streams flowing in cross-shelf troughs at the western and northern ice sheet margins (Landvik et al., 1998; Stokes and Clark, 2001; Ottesen et al., 2005; Dowdeswell et al., 2010; Fransner et al., 2018, 2017; Rebesco et al., 2014b). These paleo-ice streams are similar in size and velocity pattern to the ice streams draining the present-day WAIS. In the south-western Barents Sea, Bjørnøyrenna hosted the Bjørnøyrenna ice stream (Fig. 1), the largest ice stream draining the ice sheet during the LGM (Andreassen and Winsborrow, 2009; Bjarnadóttir et al., 2014). Data suggest that the Bjørnøyrenna ice stream had several tributaries extending into the central Barents Sea (Sentralbankrenna in the east and Storbankrenna in the north, Fig. 1) and throughout deglaciation the ice stream experienced changes in flow regime and spatial switch of their flow (Bjarnadóttir et al., 2014; Piasecka et al., 2016; Esteves et al., 2017; Newton et al., 2017). North of Bjørnøyrenna, the Storfjorden ice stream extended up to the south-western Barents Sea continental shelf edge on at least three occasions during the last 200 kyrs (Llopart et al., 2015), including the LGM (Fig. 1) (Pedrosa et al., 2011; Lucchi et al., 2013). Both the glacial drainage area and size of Storfjorden ice stream are relatively small compared to the Bjørnøyrenna ice stream (Svendsen et al., 2004), and geophysical evidence suggest a strong climatic control on its deglaciation (Lucchi et al., 2013; Nielsen and Rasmussen, 2018; Shackleton et al., 2019). During the LGM, the northern margin of the Barents Sea was drained by several ice streams, with variable size and drainage area, flowing in cross-shelf troughs/channels (Svendsen et al., 2004; Landvik et al., 1998; Dowdeswell and Siegert, 1999). In Kvitøya Trough (Fig. 1), streamlined landforms indicate the presence of warm-based, fast-flowing ice, although modest elongation ratios suggest that ice-flow velocities were relatively low compared to other drainage systems (Hogan et al., 2010a). Signatures of fast ice flow are more prominent in Franz Victoria Trough, indicating the presence of a major ice stream (Kleiber et al., 2000; Ottesen et al., 2005; Polyak et al., 1997; Hogan et al., 2010b) (Fig. 1). Further east, limited data from St. Anna Trough suggest that an ice stream occupied the entire trough to the continental shelf edge during the LGM (Polyak et al., 1997) (Fig. 1). However, the lack of bathymetric data from the north-eastern Barents Sea and Kara Sea limits the current understanding of the ice sheet dynamics in St. Anna Trough, as well as further east in Voronin Trough (Hughes et al., 2016; Patton et al., 2015).

3. Methods

3.1. Ice sheet model description

The ice sheet model used in this study is the 3D zero-order (Kirchner et al., 2011) thermo-mechanical model GRISLI (Grenoble Ice Shelf and Land Ice model, (Ritz et al., 2001)). GRISLI is a hybrid shallow ice/shallow shelf approximation model, able to simulate inland ice, ice streams, and floating ice shelves. The stress regime is determined using the Shallow Ice Approximation (SIA) (Hutter, 1983; Morland, 1984) for inland ice, whereas in ice shelves and ice streams the ice deforms according to the Shallow-Shelf Approximation (SSA) and the “dragging ice shelf” extension of the SSA, respectively (Kirchner et al., 2011; MacAyeal, 1989). During runtime, GRISLI identifies ice shelf grid points according to a simple flotation criterion based on Archimedes’ principle. Ice streams grid points are characterized by thick sediment layers saturated by meltwater and areas with low effective basal pressure (Ritz et al., 2001). The surface mass balance (SMB) over the ice sheet is computed from the annual mean temperature and precipitation using the Positive-Degree-Days (PDD) semi-empirical method (Reeh, 1991). GRISLI has been validated over Antarctica (Ritz et al., 2001) and applied over multi-millennial timescales to simulate ice inception over Eurasia during the Early Weichselian (Peyaud et al., 2007). The model version used in this study is described in (Ritz et al., 2001) and includes the improvements presented in (Peyaud et al., 2007). Below, we summarise further modifications we applied to the ice sheet model, whereas for a detailed, comprehensive description of the ice sheet model used in this study we refer to (Petrini, 2017). Finally, it is highlighted for clarity that the GRISLI version and the perturbed physics ensemble of simulations described in this study are the same as in (Petrini et al., 2018). However (Petrini et al., 2018), analyze only one ensemble member showing the best fit against the ICE-5G reconstruction (Peltier, 2004). In this study, we analyze a different group of simulations, showing the largest agreement with the data-based deglacial chronologies from the DATED-1 archive (Hughes et al., 2016) (see Subsection 3.6).

• The annual snow accumulation (ACC) is computed from the annual mean total precipitation (P_a) following a precipitation conversion scheme from (Marsiat, 1994). In this formulation, a linear transition between solid and liquid precipitation depending on the annual mean air temperature (T_a) is assumed, yielding

$$ACC = I_f \cdot P_a, \tag{1}$$

where I_f is the solid/liquid precipitation fraction, defined as

$$I_f = \begin{cases} 1, & \text{if } T_a \leq -10 \text{ }^\circ\text{C}, \\ (7 \text{ }^\circ\text{C} - T_a)/17 \text{ }^\circ\text{C}, & \text{if } -10 \text{ }^\circ\text{C} < T_a \leq 7 \text{ }^\circ\text{C}, \\ 0, & \text{if } T_a > 7 \text{ }^\circ\text{C}. \end{cases} \tag{2}$$

• The PDD method is highly sensitive to the daily temperature standard deviation (σ), a parameter accounting for the temperature daily cycle (Reeh, 1991; Braithwaite, 1984). However, this parameter is not very well constrained and previous modelling studies focusing on the Greenland ice sheet assigned to σ a single value ranging between 2.5–5.5 $^\circ\text{C}$ (Greve, 2005; Greve et al., 2011; Goelzer et al., 2011; Sundal et al., 2011). In this study, we consider the standard deviation of air temperature as a 3D variable by using an empirical parametrisation based on data from automatic weather stations in Greenland (Fausto et al., 2011). The annual mean (σ_a) and July (σ_j) standard deviations of air temperature increase with the altitude (h) and also have a minor dependence on latitude (φ),

$$\sigma_a = 0.324 + 1.104 \cdot h + 0.0573 \cdot \varphi, \tag{3}$$

$$\sigma_j = 2.220 + 1.259 \cdot h - 0.0178 \cdot \varphi. \tag{4}$$

Given σ_a and σ_j , the standard deviation of air temperature σ is assumed to vary sinusoidally over time,

$$\sigma(t) = \sigma_a + (\sigma_j - \sigma_a) \cos \frac{2\pi t}{A}, \tag{5}$$

where A is one year. Once that σ is computed, the number of PDD is obtained using the standard formulation (Reeh, 1991).

• In the original PDD formulation (Reeh, 1991), the melt factors for snow (C_s) and ice (C_i) are assumed as constant in space and time. Here, we follow (Fausto et al., 2009; Tarasov and Richard Peltier, 2002) by introducing melt factors depending on the July mean air temperature T_j ,

$$C_i = \begin{cases} 17.22 \text{ mm/PDD}, & \text{if } T_j \leq -1 \text{ }^\circ\text{C}, \\ 0.0067 \cdot (10 - T_j)^3 + 8.3 \text{ mm/PDD}, & \text{if } -1 \text{ }^\circ\text{C} < T_j \leq 10 \text{ }^\circ\text{C}, \\ 8.3 \text{ mm/PDD}, & \text{if } T_j > 10 \text{ }^\circ\text{C}, \end{cases}$$

$$C_s = \begin{cases} 2.65 \text{ mm/PDD}, & \text{if } T_j \leq -1 \text{ }^\circ\text{C}, \\ 0.15 \cdot T_j + 2.8 \text{ mm/PDD}, & \text{if } -1 \text{ }^\circ\text{C} < T_j \leq 10 \text{ }^\circ\text{C}, \\ 4.3 \text{ mm/PDD}, & \text{if } T_j > 10 \text{ }^\circ\text{C}. \end{cases} \tag{6}$$

By using this formulation, we take into account the decrease/increase of the ice and snow melt factors with temperature due to the changing mix of radiative and turbulent surface energy fluxes (Tarasov and Richard Peltier, 2002).

• Following (Pollard and DeConto, 2012), we use a parametrisation of the sub-shelf melting as a function of the far-field (*i.e.*, outside of ice-shelf cavities) ocean temperature and salinity. This empirical formulation (Holland et al., 2008) assumes a quadratic, local dependence of the sub-shelf melting rates on the heat exchanges at the ice-ocean boundary. The positive feedback between the sub-shelf melting and the circulation in ice-shelf cavities is taken into account via the quadratic relationship (Holland et al., 2008). This formulation has been used in stand-alone ice sheet simulations and has shown a good agreement with coupled ocean-ice sheet simulations under idealised future ocean warming scenarios (Favier et al., 2019). The ice temperature at the ice-shelf draft (z_b , in meters) follows from the state equation of seawater freezing point (T_f),

$$T_f(z_b) = 0.0939 - 0.057 \cdot S_o(z_b) - 7.64 \cdot 10^{-4} \cdot z_b, \tag{7}$$

where S_o is the ambient ocean salinity. Given the ambient ocean temperature (T_o), the quadratic, local ocean thermal forcing H_f is obtained,

$$H_f = (T_o(z_b) - T_f(z_b)) \cdot |T_o(z_b) - T_f(z_b)|, \tag{8}$$

and used to compute the sub-shelf melting rate as follows,

$$b_m = \frac{\rho_0 c_o \gamma_t F_m}{\rho_i L_i} \cdot H_f, \tag{9}$$

where ρ_0 is the ocean water density, $c_o = 3974 \text{ Jkg}^{-1} \text{ }^\circ\text{C}^{-1}$ is the specific heat capacity of the ocean mixed layer, $\gamma_t = 1 \times 10^4 \text{ m s}^{-1}$ is the ocean thermal exchange velocity, $\rho_i = 917 \text{ kg m}^{-3}$ is the ice density and $L_i = 3.35 \times 10^5 \text{ Jkg}^{-1}$ is the ice latent heat capacity. Our choice of the values assigned to the dimensionless model parameter F_m does not follow (Pollard and DeConto, 2012) and deserves a

separate discussion (see [Subsection 3.5](#)).

3.2. Boundary conditions

All the simulations are performed using a horizontal resolution of 20 km on a regular rectangular grid covering the Eurasian domain (210×270 gridcells). Boundary conditions are regridded onto a Lambert Equal Area geographical projection centered on the North Pole (0°E , 90°N), and include:

- Pre-Industrial (1850 a.d., PI) surface topography and bedrock elevation, based on the International Bathymetric Chart of the Arctic Ocean (IBCAO) dataset ([Jakobsson, 2014](#));
- LGM surface topography, ice thickness and bedrock elevation, based on the ICE-5G glacio-isostatic reconstruction ([Peltier, 2004](#));
- Geothermal heat flux map from ([Shapiro and Ritzwoller, 2004](#)) and sediment thickness map from ([Laske, 1997](#)).

The use of the ICE-5G reconstruction ([Peltier, 2004](#)) instead of more recent glacio-isostatic reconstructions (e.g. ICE-6G ([Peltier et al., 2015](#)), GLAC-1d ([Tarasov et al., –](#))) ensure consistency between the LGM boundary conditions and the climate forcing (see [Subsections 3.3, 3.4.1](#)). In fact, ICE-5G surface topography, ice thickness and bedrock elevation are also used in the LGM climate simulation used to force GRISLI ([Braconnot et al., 2012](#)). Finally, during runtime the isostatic bedrock response to the ice load is computed as a prognostic variable with the Elastic Lithosphere-Relaxed Asthenosphere (ELRA) method ([Le Meur and Huybrechts, 1996](#)).

3.3. Spin-up simulation setup

In order to initialise the thermodynamical state of the ice sheet, we run a 100 kyrs-long transient spin-up simulation between 122 ky BP (MIS5e) and the LGM. We assume that at MIS5 both topography and climatology were close to PI conditions, similarly as in ([Peyaud et al., 2007](#); [Patton et al., 2016](#)). Therefore, at the beginning of the spin-up simulation we prescribe the IBCAO ([Jakobsson, 2014](#)) PI bedrock elevation and the PI climatology (30-years averaged annual/July mean air temperature and annual mean precipitation), simulated with the IPSL-CM5A-LR Atmosphere-Ocean General Circulation Model (AOGCM, ([Braconnot et al., 2012](#)), [Fig. 2](#)). The PI climate fields are downscaled from the AOGCM global grid onto the ice sheet model Eurasian grid using the IBCAO ([Jakobsson, 2014](#)) PI surface topography. During the spin-up simulations, the climate forcing is progressed from PI to LGM conditions by means of a normalized climate index based on the NGRIP $\delta^{18}\text{O}$ record ([Andersen et al., 2004](#)). The LGM climatology (30-years averaged annual/July mean air temperature and annual mean precipitation) simulated with the same IPSL-CM5A-LR AOGCM ([Braconnot et al., 2012](#)) ([Fig. 2](#)) is downscaled using the ICE-5G surface elevation ([Peltier, 2004](#)) and prescribed for the last 1000 years of the simulation. During the spin-up simulation, the sea level is progressed from 0 to -125 m, using again a normalized climate index based on the NGRIP $\delta^{18}\text{O}$ record ([Andersen et al., 2004](#)). The sub-shelf melting is kept constant and equal to 0.1 m/yr, in order to allow the expansion of grounded ice over the Barents and Kara seafloors. Values of the main ice sheet model parameters in the spin-up simulation are listed in [Table 1](#).

3.4. Transient simulations setup

3.4.1. Climate forcing

In all the transient simulations of the last deglaciation presented in this study, the downscaled LGM and PI climatology simulated with the IPSL-CM5A-LR AOGCM ([Braconnot et al., 2012](#)) ([Fig. 2](#)) are prescribed as initial and final climate snapshots, respectively. During runtime, the climatology is progressed from LGM to PI conditions using different indexes for annual mean temperature and precipitation ([Fig. 3A](#)). The indexes, which are taken as representative of three macro-regions (Fennoscandia, Svalbard/Barents Sea and Siberia/Kara Sea, see Supplementary Materials in ([Petrini et al., 2018](#))), are derived from the non-accelerated transient climate simulation of the last 21 kyrs, TraCE21ka ([Liu et al., 2009](#)). Indices are normalized and vary between 1 and 0 for LGM and PI, respectively. The surface-elevation feedback is parametrised using the topographic lapse-rate (λ) and elevation-desertification (γ) factors, which correct the annual mean temperature and precipitation, respectively, for changes in elevation ([Charbit et al., 2002](#); [Marshall et al., 2007](#)). At a given time-step t , the annual mean temperature and precipitation are then obtained as follows,

$$T_a(t) = T_{\text{LGM}} \cdot i(t) + T_{\text{PI}} \cdot (1 - i(t)) - \lambda \cdot (s(t) - s_{\text{LGM}}),$$

$$P_a(t) = P_{\text{PI}} \cdot \left[\left(\frac{P_{\text{LGM}}}{P_{\text{PI}}} - 1 \right) \cdot i(t) + 1 \right] \cdot \exp(\gamma \lambda \cdot (s(t) - s_{\text{LGM}})),$$
(10)

where i is one of the different climate indexes used in this study and s is the surface elevation. The values of the topographic lapse-rate and elevation-desert factors used in the transient simulations are not the same as in the spin-up simulation and are discussed in [Section 3.5](#). Our choice of using the TraCE21ka simulation ([Liu et al., 2009](#)) to derive macro-regional climate indexes only is motivated by the fact that the LGM climatology simulated with the IPSL-CM5A-LR AOGCM ([Braconnot et al., 2012](#)) provided the best fit between the simulated and reconstructed ([Hughes et al., 2016](#)) Eurasian ice sheets at the LGM.

3.4.2. Ocean forcing

In all the transient simulations of the last deglaciation presented in this study, we force the two-equation sub-shelf melting formulation (see [Section 3.1](#)) with four different time-varying vertical profiles of annual mean ocean temperature and salinity, derived from the non-accelerated transient climate simulation of the last 21 kyrs, TraCE21ka ([Liu et al., 2009](#)). Similarly as for the atmospheric indexes, the ocean temperature and salinity vertical profiles are taken as representative of four macro-regions (Norwegian Sea, south-western and north-western Barents Sea and southern Arctic Ocean, see Supplementary Materials in ([Petrini et al., 2018](#))). Ocean vertical profiles representative of the south-western and north-western Barents Sea are prescribed at the south-western and north-western ice sheet margins, respectively, whereas at the northern margin of the ice sheet we force the sub-shelf melting formulation with ocean vertical profiles representative of the southern Arctic Ocean. Using these ocean temperature and salinity profiles, ocean thermal forcings and basal melt rates are computed at each time step (Eqs. (7)–(9)) at five different depth layers (-2 m, -200 m, -400 m, -600 m, -800 m) and then vertically interpolated. Time-series of the ocean thermal forcing in the Barents Sea (average between south-western and north-western

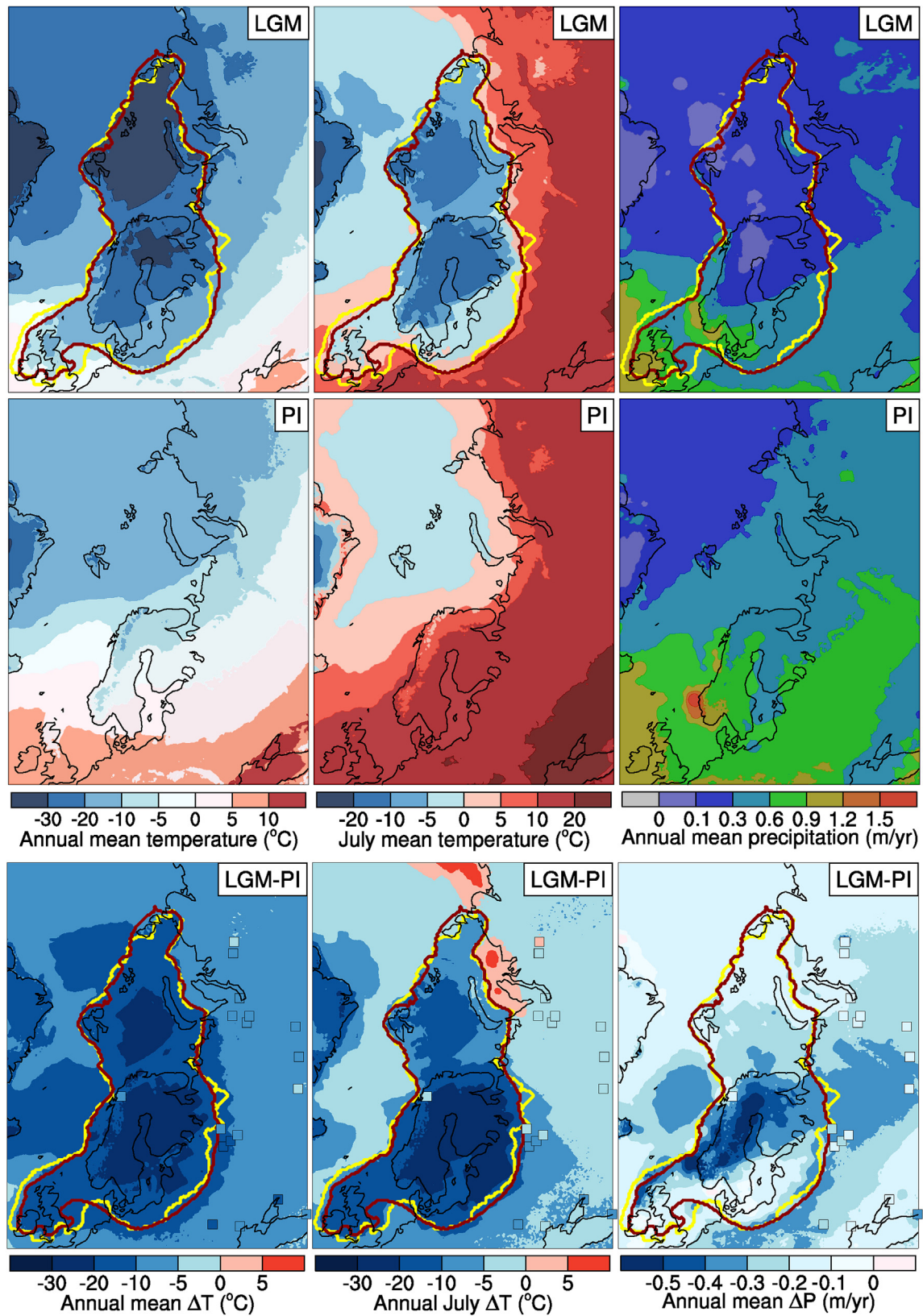


Fig. 2. Reference climatology simulated with the IPSL-CM5A-LR AOGCM (Braconnot et al., 2012) interpolated into the ice sheet model grid. Top panels show annual mean temperature, July mean temperature and annual mean precipitation (left to right) at the LGM, whereas in the central panels the same fields are shown for PI. In the bottom panels, LGM - PI annual mean temperature, July mean temperature and annual mean precipitation anomalies are shown. The colored squares in the bottom panels show LGM - PI anomalies based on pollen data (Bartlein et al., 2011). In the top panels and bottom panels, red and yellow lines show the LGM ice sheet extent simulated in this study and from the ICE-5G reconstruction, respectively. (For interpretation of the references to color in this figure legend, the reader is referred to the Web version of this article.)

Table 1

List of GRISLI model parameters. The parameters marked with a star refer to the spin-up simulation only, whereas their range of values in the transient simulations of the last deglaciation is listed in Table 2.

Symbol	Description	Units	Value
E_{SIA}^*	SIA enhancement factor	—	3
E_{SSA}	SSA enhancement factor	—	1
c_f^*	Basal drag coefficient	—	$2 \cdot 10^{-5}$
c_i	Ice heat capacity	J/kg ^o C	2009
κ_i	Ice thermal conductivity	J/m ^o Cs	2.1
λ^*	Lapse-rate value	°C/km	0.005
γ^*	Precipitation-correction factor	1/°C	0.05
ρ	Ice density	kg/m ³	917
K	Hydraulic conductivity	m/s	10^{-6}
H_c	Thickness threshold for the calving criterion	m	200
τ_f	Relaxation time of the astenosphere	yr	3000
f_m^*	Sub-shelf melting parameter	—	—
b_m	Sub-shelf melting rate	m/yr	0.1

sectors) and southern Arctic Ocean at different depths are shown in Fig. 3B. Finally, the sea level is progressed from -125 m (LGM) to 0 m (PI) during runtime, using a normalized index based on the NGRIP $\delta 180$ record (Fig. 3A).

3.5. Perturbed physics ensemble of transient ice sheet model simulations

A large source of uncertainty in ice sheet model simulations is the presence of semi-empirical parametrisations in the models, whose parameters spans a large range of values in the literature. In this study, instead of performing a fine-tuning of individual parameters, we use the maxi-min Latin Hypercube Sampling (mLHS) procedure to obtain random samples of $k = 5$ selected ice sheet model parameters. In this procedure, for each model parameter $n = 100$ values are randomly distributed in the intervals $(a, a + 1/n)$, $(a + 1/n, a + 2/n)$, ..., $(b - 1/n, b)$, where a and b are the lower and upper bounds, respectively, of the parameter range of values. Due to the large uncertainties regarding the selected model parameters, the n values of each parameter are chosen in such a way that the minimal distance among pairs of points is maximized. The n values of k model parameters are then randomly permuted, and the combinations of sampled parameters are used to generate a perturbed physics ensemble of 100 transient simulations of the last deglaciation. The ratio $n/k = 20$ between the number of simulations and the selected model parameters is the same adopted by (Stone et al., 2010; Applegate et al., 2015), whereas a larger number of model parameters and simulations/parameters ratio were used by (Gregoire et al., 2016; Stokes and Tarasov, 2010; Tarasov et al., 2012). Nevertheless, choosing $n/k = 20$ represents a reasonable tradeoff between minimizing the computing time and sufficiently covering the parameter space (Stone et al., 2010).

Our choice of model parameters included in the statistical sampling is related to the main mechanisms of ice loss in a marine-based ice sheet. Ice flows from the interior towards fast-flowing regions mainly due to internal deformation. In this type of flow, commonly referred to as simple-shear flow, the anisotropy of the ice plays an important role in determining the stress regime (Ma et al., 2010). In GRISLI, the SIA enhancement factor E_{SIA} accounts for the anisotropy of polycrystalline ice under condition of simple-shear flow (Ma et al., 2010). Under higher values of E_{SIA} , the ice will deform more easily, and the ice transport from the interior towards the fast-flowing regions will be more efficient. Large-scale ice sheet modelling studies adopted a range from 1 to 5 for this parameter (Stone et al., 2010; Applegate et al., 2015; Colleoni et al., 2016). However, a higher value of 5.6 is suggested in a study where

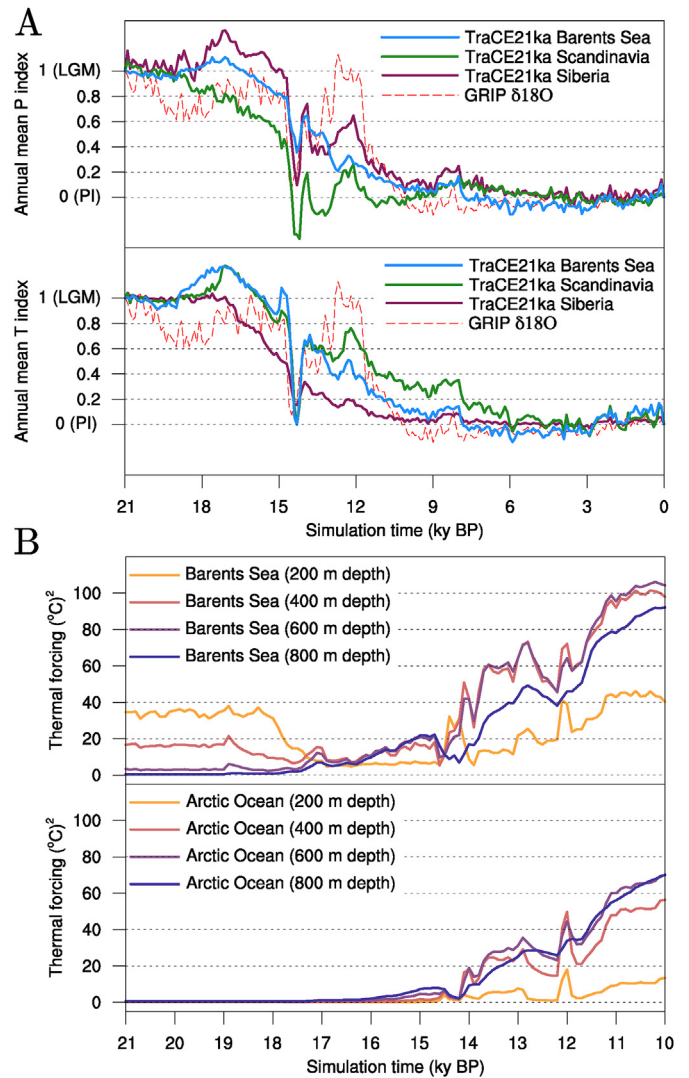


Fig. 3. (A) TraCE21ka (Liu et al., 2009) macro-regional indexes (solid lines) for annual and July mean air temperature (top panel) and annual mean precipitation (bottom panel) used to progress between LGM and PI reference climatology during the transient simulations. For comparison, the index based on the NGRIP $\delta 180$ record (Andersen et al., 2004) is shown in both panels (dashed red line). (B) Macro-regional ocean thermal forcing for the Barents Sea (top panel) and the Arctic Ocean (bottom panel) at typical grounding line depths (200, 400, 600 and 800 m) between 21 and 10 ky BP. The thermal forcing is computed based on the TraCE21ka (Liu et al., 2009) macro-regional ocean temperature and salinity profiles (see Figure S1) using Equations (7) and (8). (For interpretation of the references to color in this figure legend, the reader is referred to the Web version of this article.)

an anisotropic full-Stokes model is used (Ma et al., 2010). Therefore, in this study we select the range 1 – 5.6. In fast-flowing regions (*i.e.*, ice streams), ice is rapidly delivered to the ice sheet margins, where mass loss can occur by surface ablation, sub-shelf melting or calving. In GRISLI, the flow regime in ice streams is simulated with the “dragging ice shelf” extension of the SSA. In these regions, the SSA is combined with a friction law, $\tau_b = c_f N u_b$, where N is the effective pressure, u_b is the basal velocity and c_f is the basal drag coefficient, which regulates the resistive force acting at the ice stream base. Lower values of c_f leads to larger sliding velocities in ice streams, thus increasing the ice transport towards the ice sheet edges. This parameter was set in previous large-scale ice sheet modelling studies to $1 \cdot 10^{-5}$ (Peyaud et al., 2007), $9 \cdot 10^{-5}$ (Dumas, 2002) and between $10 \cdot 10^{-5}$ and $100 \cdot 10^{-5}$ (Álvarez Solás et al.,

2011). In this study, we explore the range $1 \cdot 10^{-5} - 100 \cdot 10^{-5}$. Ice melting at the ice sheet margins is determined by ablation and ocean melting under the ice shelves. When an ice sheet becomes thinner, ablation zones can form or expand in response to increased air temperatures due to surface elevation lowering. In this study, we parametrise this positive feedback by means of the topographic lapse-rate λ , which represents an approximation of how much the near-surface air temperature changes with elevation. Previous large-scale ice sheet modelling studies adopted a range for this parameter from 4 to $8.2^\circ\text{C}/\text{km}$ ((Stone et al., 2010; Gregoire et al., 2016; Colleoni et al., 2016), whereas climate simulations suggest a range from 4 to $7^\circ\text{C}/\text{km}$ (Abe-Ouchi et al., 2007). In this study, we explore the range $4 - 8.2^\circ\text{C}/\text{km}$. The increase in air temperatures caused by surface elevation lowering will also result in an increase in precipitation, due to the larger saturation pressure of water vapour. This negative feedback, which can partially compensate for the increase in ablation, is represented in this study via the elevation-desertification factor γ . Large-scale ice sheet modelling studies suggest a range between 0.03 and 0.078°C^{-1} for this parameter (e.g., Charbit et al., 2002), whereas climate modelling studies suggest that γ can take higher values up to 0.11°C^{-1} ((Colleoni et al., 2016) and references therein). In this study, the range $0.03 - 0.1^\circ\text{C}^{-1}$ is explored. Finally, in the sub-shelf melting formulation used in this study the magnitude of melting rates in response to the ocean thermal forcing (see Eq. (7)) is modulated by the sub-shelf melting parameter F_m . This dimensionless parameter has been previously introduced in order to match simulated and observed grounding-line position in Antarctica (Pollard and DeConto, 2012; Martin et al., 2011). However, the oceanic conditions used in (Pollard and DeConto, 2012; Martin et al., 2011) to force the sub-shelf melting parametrisation are drastically different from those used in this study (Fig. 4). Therefore, we identify a new range of values for F_m so that the sub-shelf melting rates are within the range of values observed under the present-day Antarctica ice shelves (Rignot et al., 2013; Paolo et al., 2015; Pritchard et al., 2012) (see Supplementary Materials in (Petrini et al., 2018)). The range of values explored in this study is $0.005 \cdot 10^{-3} - 1.5 \cdot 10^{-3}$. The list of GRISLI model parameters included in the mLHS in this study, with their associated range of values, is summarised in Table 2.

Our list of model parameters is slightly different from that used by (Stone et al., 2010; Applegate et al., 2015; Gregoire et al., 2016), where ice/snow melt factors and the geothermal heat flux were included in the statistical sampling. In this study, we do not consider these parameters in the sampling as they are not single-valued, with melt factors depending on the July mean air temperature and the geothermal heat flux being prescribed from a two-dimensional map (see Subsection 3.1).

3.6. Model-data comparison

In order to rule out unrealistic simulations, we test each member of the ensemble of 100 transient simulations of the last deglaciation against the data-based deglacial chronologies from the DATED-1 archive (Hughes et al., 2016). The DATED-1 archive (Hughes et al., 2016) provides time-slice most-credible, minimum and maximum (mc, min and max, respectively) reconstructions of the Eurasian ice sheets extent between 21 and 10 ky BP. Such reconstructions are based on a comprehensive collection of existing published chronological data with a census date of 1 January 2013. In the BSIS region, radiocarbon dates based on marine cores from the continental shelf and trough-mouth fans on the continental slope are combined with generalized flow patterns to reconstruct the ice sheet retreat pattern and configuration. In order to provide a quantitative comparison between the simulated and reconstructed deglaciation scenarios, all the DATED-1 reconstructions between 21

and 13 ky BP are regridded onto the ice sheet model grid. For each ensemble member, at each time slice we compute the percentage of the “total” BSIS area showing model/data agreement, overestimation and underestimation (Fig. 4B). The “total” BSIS area is defined as $A_{TOT} = (A_S \cap A_D) \cup (A_S \setminus A_D) \cup (A_D \setminus A_S)$, where A_S is the simulated area and A_D is the DATED-1 area. At each time slice, a grid cell is considered to show model/data agreement if there is agreement between the simulated scenario and at least one of the DATED-1 scenarios (mc-min-max). Otherwise, the model overestimates or underestimates the ice extent in that specific gridcell compared to the DATED-1 reconstruction. For our final analysis, we select a restricted group of nine ensemble members (“admissible simulations”) showing the largest percentage of total ice sheet area model/data agreement (Fig. 4B). These nine ensemble members satisfies the following minimal requirements of model-data agreement: (a) 21-13 ky BP average model/data agreement larger than 60% (b) minimum time slice model/data agreement larger than 40% (c) last time slice (13 ky BP) model/data agreement larger than 50%. These model/data agreement percentages are relatively low as in all the ensemble members the ice sheet extent at the eastern margin is systematically overestimated (Fig. 4A). In Subsection 4.2.2 this large model/data mismatch is carefully analyzed, and several hypothesis to explain the overestimation are proposed. In the western, central and northern Barents Sea the ice sheet extent throughout the deglaciation has a much larger variability across the ensemble, and the admissible simulations provide the best fit with the DATED-1 reconstruction (Fig. 4A). The range of values assumed by the model parameters c_f , λ and γ in the admissible simulations remains similar to the full range of values considered for the mLHS procedure, with individual values spreading across the full interval length (Fig. 5 and Table 2). In contrast, the values assumed by parameters E_{SIA} and F_m in the admissible simulations are more clustered in the second half of the full range interval (Fig. 5 and Table 2).

The nine admissible simulations are used to construct minimum (min), maximum (mc) and average (avg) simulated deglaciation scenarios every thousand years between 21 and 13 ky BP. In the next section, these scenarios are analyzed and compared with the DATED-1 min-max-mc reconstructions. In the comparison between min-max-avg simulated scenarios and the DATED-1 min-max-mc reconstructions, a grid cell is considered to show agreement between model and observations if there is agreement between at least one of the three simulated/DATED-1 scenarios. Otherwise, the simulated ice extent is either overestimated/underestimated in that specific gridcell compared to the DATED-1 reconstruction.

4. Results and discussion

4.1. Barents Sea ice sheet during the LGM

At the end of the spin-up simulation, Northern Eurasia is covered by an interconnected complex of ice sheets (Fig. 6A). The BSIS is connected to the SIS in the south and covers a total area of 2.42 Mkm^2 (Figs. 6A and 7B and Table 3). The western and northern margins of ice sheet extend up to the continental shelf break in the western and northern Barents Sea, respectively, whereas the eastern termination of the ice sheet is located in the relatively shallow central Kara Sea (Figs. 1 and 6A).

The simulated ice sheet extent is slightly underestimated (3% of the total area) with respect to the DATED-1 reconstruction (Figs. 10 and 4). The simulated grounding-line position is slightly shifted towards the interior of the ice sheet at the mouth of Kvitøya, Franz Victoria, St. Anna and Bjørnøyrenna ice streams. This underestimation can be explained by looking at the mass budget at the ice sheet western and northern margins during the LGM. The July

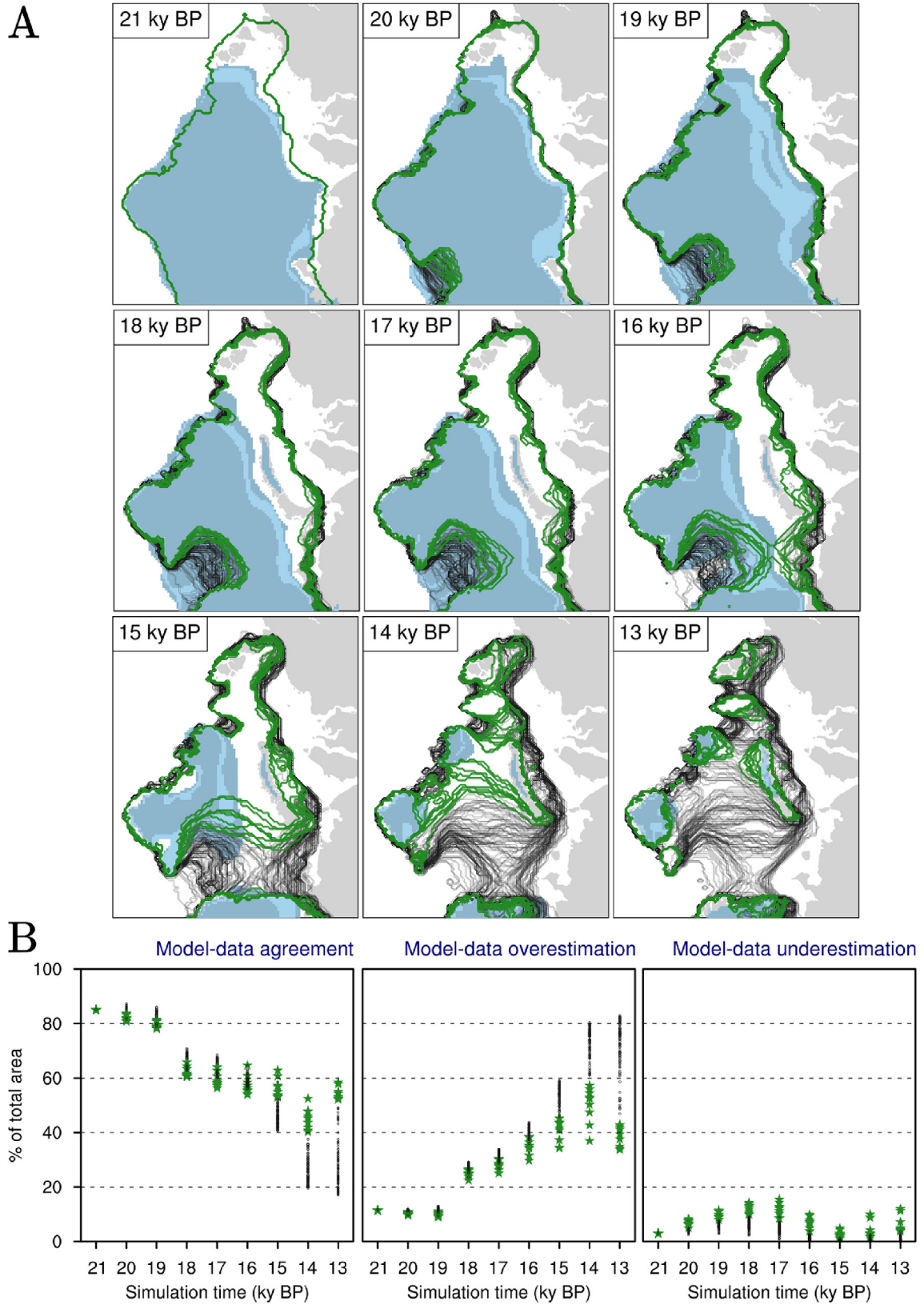


Fig. 4. (A) Evolution of the simulated BSIS at 1000 yr time-slices between 21 and 13 ky BP for all the simulations in the ensemble (black lines). Admissible simulations (see Subsection 3.6) are shown in green. In the background, the DATED-1 min-mc-max scenarios are shown in light blue. (B) Simulated/DATED-1 ice sheet area agreement (left panel), overestimation (central panel) and underestimation (right panel) for all the members of the simulations ensemble between 21 and 13 ky BP. Admissible simulations (see Subsection 3.6) are marked in green. (For interpretation of the references to color in this figure legend, the reader is referred to the Web version of this article.)

Table 2
List of GRISLI model parameters included in the mLHS, with their associated "Full Ensemble"/"Admissible Simulations" range of values ("FE" Range/"AS" range) and average value ("FE" avg/"AS" avg).

Symbol	"FE" Range	"FE" Avg	"AS" range	"AS" avg
λ	[4 – 8.2]	6.1	[5.0 – 7.8]	6.5
γ	[0.03 – 0.1]	0.065	[0.05 – 0.1]	0.082
E_{SIA}	[1 – 5.6]	3.3	[3.6 – 5.4]	4.8
c_f	$[1 – 10] \cdot 10^{-5}$	$5 \cdot 10^{-5}$	$[2 – 10] \cdot 10^{-5}$	$4 \cdot 10^{-5}$
f_m	$[0.005 – 1.5] \cdot 10^{-3}$	$0.8 \cdot 10^{-3}$	$[0.6 – 1.5] \cdot 10^{-3}$	$1.2 \cdot 10^{-3}$

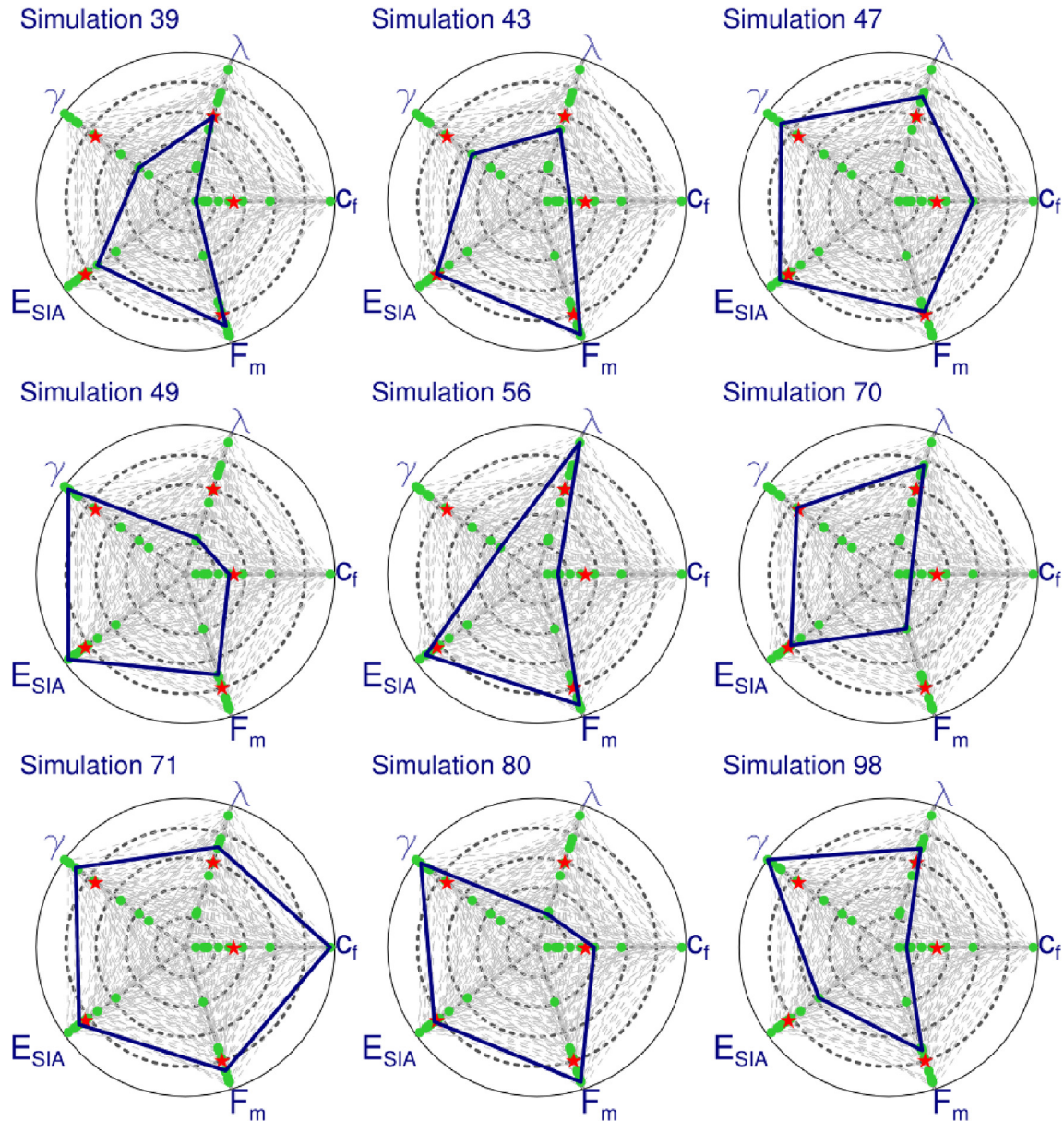


Fig. 5. Radar plots showing the model parameters position within each range of values (normalized between 0, corresponding to the minimum values, and 1, corresponding to the maximum values, see Table 2) for all the admissible simulations (see Subsection 3.6). In each plot, the green polygon indicates the model parameters position relative to the individual simulation, whereas the green dots refer to the parameters position in the remaining admissible simulations. The red dots show the average parameter values in the admissible simulations, and the dashed grey polygons in the background show the combinations of model parameters for all the simulations in the ensemble. (For interpretation of the references to color in this figure legend, the reader is referred to the Web version of this article.)

mean air temperature remains below -5°C in the region covered by the BSIS (Fig. 2), thus preventing the formation of ablation zones. The sub-shelf melting is set to a constant, low value of 0.1 myr^{-1} and the mean annual precipitation is lower than 0.3 myr^{-1} .

Therefore, the mass budget over the floating ice shelves at the ice streams mouth is either slightly positive or negative and prevents the floating ice proximal to the grounding-line to thicken enough to become grounded (see Fig. 6A and B). In addition, the eustatic sea

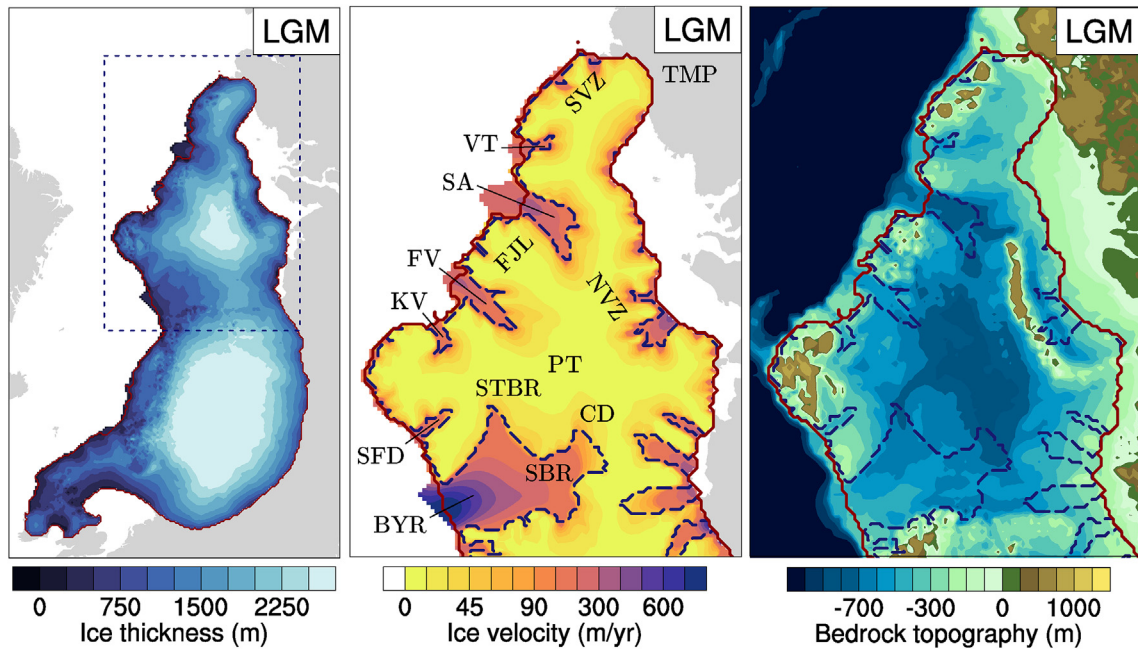


Fig. 6. (A) Ice thickness of the simulated Eurasian ice sheets at the LGM. The blue dashed line indicates the region showed in panels (B) and (C). (B) Simulated ice velocities of the BSIS at the LGM. The blue dashed line indicates the boundary between regions treated with the SSA (ice streams and floating ice shelves) and with the SIA (inner part of the ice sheet) at the LGM. For clarity, we add abbreviations of the main geographic locations as follows: BYR = Bjørnøyrenna, SBR = Sentralbankrenna, CD = Central Deep, STBR = Storbankrenna, PT = Persey Trough, SFD = Storjordrenna, KV = Kvitøya Trough, FV = Franz Victoria Trough, SA = St. Anna Trough, VT = Voronin Trough, FJL = Franz Josef Land, NVZ = Novaya Zemlya, SVZ = Severnaya Zemlya, TMP = Taimyr Peninsula. (C) Simulated isostatically depressed bedrock topography at the LGM in the BSIS region. Blue dashed line as in panel (B). In all the panels, the red line indicates the LGM simulated grounded ice limit. (For interpretation of the references to color in this figure legend, the reader is referred to the Web version of this article.)

level prescribed at the LGM (-125 m) does not account for spatial variability in relative sea level. A lower relative sea level at the mouth of Kvitøya, Franz Victoria, St. Anna troughs and Bjørnøyrenna would therefore allow the ice stream front to extend up to the continental shelf edge.

The simulated ice sheet extent overestimation relative to DATED-1 is the 12% of the total ice sheet area, mainly due to an excess of ice covering Severnaya Zemlya and impinging onto Taimyr Peninsula at the north-eastern margin (Figs. 1, Figs. 10 and 4). The presence of this overestimated ice lobe is strictly linked with the LGM temperature and precipitation simulated with the IPSL-CM5A-LR AOGCM (Braconnot et al., 2012) (Fig. 2). Although the annual mean precipitation is relatively low in this area, ranging between 0.1 and 0.3 myr^{-1} , the annual surface mass balance remains positive as July mean air temperatures remain below -5°C , thus preventing summer ablation. It is interesting to note that in the immediate vicinity of the north-eastern and eastern ice sheet margin, July mean air temperatures are above zero and range from 0 to 5°C (Fig. 2). Therefore, we claim that the negative LGM July mean air temperature simulated with the IPSL-CM5A-LR AOGCM (Braconnot et al., 2012) over the north-eastern ice sheet margin are caused by the use of the ICE-5G (Peltier, 2004) LGM ice sheet extent/thickness in the climate model. In fact, also in the ICE-5G reconstruction an ice lobe more than 800 m thick is covering Severnaya Zemlya and the coast of Taimyr Peninsula, thus largely overestimating the surface topography in this area with respect to what recent reconstructions suggest (Hughes et al., 2016). The ice extent overestimation at the LGM is also observed in both ICE-6G (Peltier et al., 2015) and GLAC-1d (Tarasov et al., –) glacioisostatic reconstructions, and currently there are no published reconstructions based on GIA models correcting the ice sheet extent in the north-east. The boundary between strong negative (less than -5°C) and positive July mean air temperatures matches

exactly the ICE-5G ice sheet eastern limit (Fig. 2), suggesting that also at the eastern margin the ICE-5G ice thickness may play a role in overestimating the LGM cooling in the climate model (Braconnot et al., 2012). Looking at the simulated LGM annual mean air temperatures (Braconnot et al., 2012), a cooling between -10 and -20°C is observed with respect to PI (Fig. 2) at the north-eastern and eastern ice sheet margins. Pollen-based reconstructions from the North Siberian Lowland suggest a lower LGM cooling ranging between -4 and -10°C (Bartlein et al., 2011) (Fig. 2). Outside the ice sheet eastern and north-eastern margins the LGM-PI annual mean air temperature cooling simulated with the IPSL-CM5A-LR climate model (Braconnot et al., 2012) has a similar range compared to proxy reconstruction (Fig. 2). Finally, previous modelling studies showed that the PDD method tends to underestimate surface ablation (Sergienko and Macayeal, 2005; Pritchard et al., 2008). Therefore, the impact of a cold bias at the north-eastern and eastern ice sheet margins during the LGM could be possibly amplified by the simplified method used in this study to compute surface ablation.

4.2. Last deglaciation of the BSIS

4.2.1. Early western margin retreat between 21 and 18 ky BP

Between 21 and 19 ky BP, the BSIS loses around 0.34 Mkm^2 of ice cover at a rate between 150 and 180 km^2/yr (Fig. 7 and Table 3). More than a half of this initial area loss is due to the simulated retreat of the Bjørnøyrenna ice stream at the western ice sheet margin, which register an area loss of 0.23 Mkm^2 (Fig. 8 and Table 3). Between 21 and 20 ky BP, the ice stream front retreats from the outer to the central trough, and by 19 ky BP the central branch of Bjørnøyrenna ice stream reaches the outer part of Sentralbankrenna (Fig. 9). Between 19 and 18 ky BP, the ice sheet loses 0.15 Mkm^2 of ice cover, at a rate of 150 km^2/yr (Fig. 7 and Table 3).

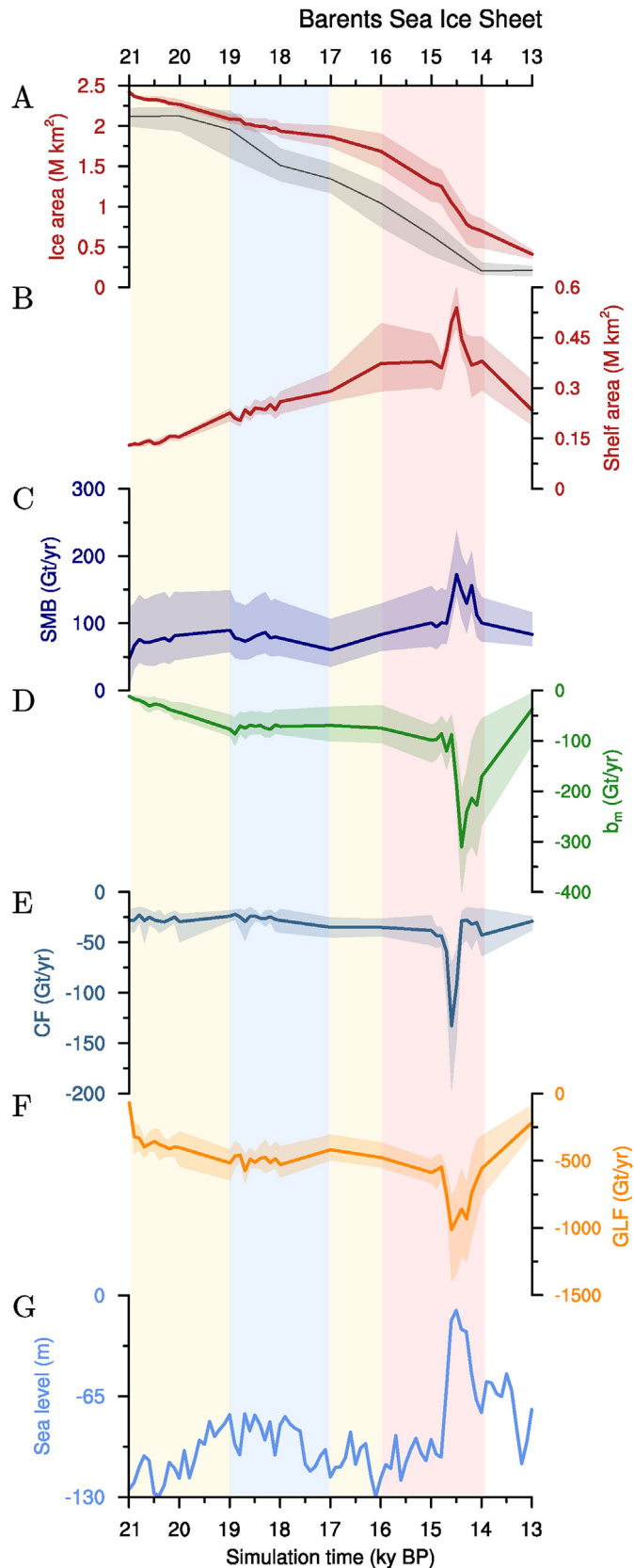


Fig. 7. Time series of integrated (a) ice area, (b) ice shelf area, (c) SMB, (d) sub-shelf melting, (e) calving flux, (f) grounding-line flux for the BSIS in the minimum, maximum (shading) and average (solid lines) simulated scenario (see Subsection 3.6). The eustatic sea level prescribed in all the simulations of the ensemble is shown in (f).

The western ice sheet margin show an area loss of 0.11 Mkm² (Fig. 8 and Table 3), with the Bjørnøyrenna ice stream further retreating towards the inner part of the trough (Fig. 9). Between 20 and 18 ky BP, the simulated grounding-line position at the mouth of Bjørnøyrenna ice stream is shifted up to 50 km towards the inner/outer part of the trough in the minimum/maximum simulated scenarios, respectively (Fig. 9). At the northern ice sheet margin, in all three simulated scenarios the Kvitøya, Franz Victoria, Voronin and St. Anna ice streams show a limited retreat during this initial phase (Fig. 9). The overall area loss at the northern ice sheet margin is 0.1 Mkm² in three thousand years, with relatively low retreat rates ranging between 40 and 50 km²/yr (Fig. 8 and Table 3).

The relatively low simulated retreat of the ice streams at the northern ice sheet margin cannot be directly linked to climatic factors, as between 21 and 15 ky BP the SMB remains positive and the sub-shelf melting is close to zero (Fig. 9). In fact, during this time interval annual and July mean air temperatures over the Barents and Kara seas remain at their LGM values, and the Arctic Ocean thermal forcing is close to zero (Fig. 3A and B). Therefore, this slow, steady retreat can only be explained by an unstable response of the ice streams to the initial sea level rise prescribed after the LGM. Inside the deep, retrograde-sloping troughs at the northern ice sheet margin, the ice thickness at the grounding-line is close to its flotation threshold during the LGM (see Fig. 6A and C). The sea level increase prescribed after 21 ky BP causes grounded ice to become afloat and accelerate, as a result of the sudden lack of basal drag. This can lead to a further increase in the longitudinal stresses upstream, causing in turn further thinning at the grounding-line, which already migrated inland where the trough is deeper. However, this process is not irreversible and is stopped when the grounding-line retreats inland into a region with higher ice thickness, well above the flotation threshold. For this reason, the simulated retreat of the northern margin ice streams between 21 and 18 ky BP is relatively slow and only cause the grounding-line to recede from the outer into the inner troughs. Both observations and ice sheet modelling studies showed that sea level rise alone is capable of initiating relatively slow, episodic ice retreat events (Mackintosh et al., 2011; Cofaigh et al., 2019).

The initial simulated retreat of Bjørnøyrenna ice stream is much larger than those simulated at the northern ice sheet margin and therefore cannot be explained by sea level rise alone. Even though both the western and northern margins share a similar, positive SMB (Fig. 8), the oceanic forcing at the two margins are drastically different (Fig. 3B). Between 21 and 19 ky BP, the ice loss at the western margin due to sub-shelf melting rapidly increase, reaching values of 76 Gt/yr (Fig. 8 and Table 3). This increase can be explained by the relatively high ocean thermal forcing prescribed between 200 and 400 m depth, due to the presence of warm subsurface Atlantic water (Fig. 3B). Even though this warm ocean layer does not fully reach grounding-line depths within the trough (Fig. 1), it is deep enough to cause prolonged ice shelf thinning and grounding-line retreat. Between 19 and 17 ky BP, the integrated ice loss at the western ice sheet margin due to sub-shelf melting slightly decreases, in spite of the increase in ice shelf area (Fig. 8 and Table 3). This can be explained by a reduction in the ocean thermal forcing prescribed at 400 and, to a less extent, at 200 m depth (Fig. 3B) due to the AMOC gradual weakening in the TraCE21ka simulation (Liu et al., 2009). This decrease in sub-shelf melting at the western margin corresponds to a slowdown in the rate of ice area loss (Fig. 8 and Table 3), thus suggesting that the oceanic forcing played a primary role in modulating the initial retreat of the western ice sheet margin.

The early simulated retreat of the Bjørnøyrenna ice stream and, to a less extent, of other major ice streams (Kvitøya, Franz Victoria and St. Anna) at the northern ice sheet margin is larger than in the

Table 3

Integrated ice volume, sea level rise rate, ice area, rate of ice area loss, ice shelf area and sub-shelf melting throughout the deglaciation in the average simulated scenario.

Time	Ice volume	SLR rate	Ice area	Rate of area loss	Shelf area	Sub-shelf melting
Barents Sea ice sheet						
21 ky BP	8.74 m SLE	–	2.42 Mkm ²	–	0.13 Mkm ²	12 Gt/yr
20 ky BP	7.98 m SLE	0.75 mm/yr	2.27 Mkm ²	150 km ² /yr	0.15 Mkm ²	44 Gt/yr
19 ky BP	7.10 m SLE	0.88 mm/yr	2.08 Mkm ²	180 km ² /yr	0.23 Mkm ²	77 Gt/yr
18 ky BP	6.20 m SLE	0.90 mm/yr	1.94 Mkm ²	150 km ² /yr	0.26 Mkm ²	72 Gt/yr
17 ky BP	5.44 m SLE	0.75 mm/yr	1.86 Mkm ²	70 km ² /yr	0.29 Mkm ²	69 Gt/yr
16 ky BP	4.62 m SLE	0.82 mm/yr	1.69 Mkm ²	180 km ² /yr	0.37 Mkm ²	75 Gt/yr
15 ky BP	3.36 m SLE	1.27 mm/yr	1.29 Mkm ²	390 km ² /yr	0.38 Mkm ²	100 Gt/yr
14.4 ky BP	2.17 m SLE	1.97 mm/yr	0.88 Mkm ²	690 km ² /yr	0.45 Mkm ²	310 Gt/yr
14 ky BP	1.40 m SLE	1.95 mm/yr	0.70 Mkm ²	450 km ² /yr	0.38 Mkm ²	171 Gt/yr
13 ky BP	0.45 m SLE	0.94 mm/yr	0.41 Mkm ²	290 km ² /yr	0.23 Mkm ²	37 Gt/yr
Western/Central Barents Sea						
21 ky BP	5.57 m SLE	–	1.47 Mkm ²	–	0.04 Mkm ²	5 Gt/yr
20 ky BP	5.09 m SLE	0.48 mm/yr	1.37 Mkm ²	110 km ² /yr	0.06 Mkm ²	44 Gt/yr
19 ky BP	4.47 m SLE	0.61 mm/yr	1.24 Mkm ²	130 km ² /yr	0.12 Mkm ²	76 Gt/yr
18 ky BP	3.82 m SLE	0.65 mm/yr	1.13 Mkm ²	110 km ² /yr	0.15 Mkm ²	71 Gt/yr
17 ky BP	3.26 m SLE	0.56 mm/yr	1.07 Mkm ²	60 km ² /yr	0.19 Mkm ²	69 Gt/yr
16 ky BP	2.64 m SLE	0.62 mm/yr	0.94 Mkm ²	140 km ² /yr	0.26 Mkm ²	74 Gt/yr
15 ky BP	1.59 m SLE	1.04 mm/yr	0.61 Mkm ²	320 km ² /yr	0.25 Mkm ²	95 Gt/yr
14.4 ky BP	0.80 m SLE	1.32 mm/yr	0.35 Mkm ²	450 km ² /yr	0.25 Mkm ²	294 Gt/yr
14 ky BP	0.37 m SLE	1.07 mm/yr	0.25 Mkm ²	230 km ² /yr	0.19 Mkm ²	110 Gt/yr
13 ky BP	0.19 m SLE	0.19 mm/yr	0.20 Mkm ²	40 km ² /yr	0.08 Mkm ²	4 Gt/yr
Northern/Eastern Barents Sea						
21 ky BP	3.27 m SLE	–	0.97 Mkm ²	–	0.09 Mkm ²	8 Gt/yr
20 ky BP	2.99 m SLE	0.28 mm/yr	0.93 Mkm ²	40 km ² /yr	0.09 Mkm ²	< 1 Gt/yr
19 ky BP	2.72 m SLE	0.27 mm/yr	0.87 Mkm ²	50 km ² /yr	0.11 Mkm ²	< 1 Gt/yr
18 ky BP	2.46 m SLE	0.25 mm/yr	0.83 Mkm ²	40 km ² /yr	0.12 Mkm ²	< 1 Gt/yr
17 ky BP	2.27 m SLE	0.20 mm/yr	0.82 Mkm ²	10 km ² /yr	0.11 Mkm ²	< 1 Gt/yr
16 ky BP	2.06 m SLE	0.20 mm/yr	0.77 Mkm ²	40 km ² /yr	0.12 Mkm ²	< 1 Gt/yr
15 ky BP	1.84 m SLE	0.23 mm/yr	0.70 Mkm ²	70 km ² /yr	0.13 Mkm ²	5 Gt/yr
14.4 ky BP	1.42 m SLE	0.69 mm/yr	0.55 Mkm ²	255 km ² /yr	0.20 Mkm ²	20 Gt/yr
14 ky BP	1.04 m SLE	0.95 mm/yr	0.46 Mkm ²	220 km ² /yr	0.20 Mkm ²	70 Gt/yr
13 ky BP	0.26 m SLE	0.78 mm/yr	0.21 Mkm ²	250 km ² /yr	0.16 Mkm ²	32 Gt/yr

DATED-1 min-mc-max scenarios, leading to an increase in the ice area underestimation up to 0.2 Mkm² (8–10% of the total ice sheet area, Fig. 10 and Table 4). In the DATED-1 reconstruction, the Kvitøya, Franz Victoria and St. Anna ice streams front position remains unchanged until 19 ky BP. By this time, the simulated ice streams at the northern ice sheet margin already started to slowly, steadily retreat (Fig. 10). After 19 ky BP, the DATED-1 reconstruction suggests that the ice streams at the northern ice sheet margin started to retreat into the inner trough, and from 17 ky BP onwards the simulated and DATED-1 northern margin extent are in good agreement (Fig. 10). In the DATED-1 scenarios, the Bjørnøyrenna ice stream does not retreat significantly from the continental shelf edge between 21 and 19 ky BP. Only during the following two thousand years the southern branch of the ice stream recedes in the inner part of Bjørnøyrenna. The mismatch between the simulated and reconstructed Bjørnøyrenna ice stream front position is already large at 20 ky BP and peaks at 18 ky BP (Fig. 10 and Table 4).

The model-data mismatch at the western and northern ice sheet margin between 21 and 18 ky BP can be explained by several factors. First, the coarse horizontal resolution (20 km) used in this study might amplify the grounding-line response to both ice shelf thinning and increase in the prescribed sea level. Moreover, the size of the simulated Bjørnøyrenna ice stream during the LGM (Fig. 6B) is larger, especially in the south, than what marine geophysical data suggest (Andreassen and Winsborrow, 2009; Bjarnadóttir et al., 2014; Piasecka et al., 2016; Esteves et al., 2017; Newton et al., 2017). In this regard, the method used in GRISLI to identify ice stream areas (presence of thick sediment layers saturated by meltwater (Peyaud et al., 2007)) and to parametrise subglacial hydrology (based on a simple hydraulic gradient model (Peyaud et al., 2007)) might favor the formation of large ice streams in topographic depressions. An overestimation of the Bjørnøyrenna

ice stream area can amplify the fast and unstable response to ice shelf thinning and sea level rise, although it is difficult to properly quantify such an amplification. Another factor is related to the TraCE21ka ocean forcing prescribed at the western Barents Sea margin between 21 and 18 ky BP (Supplementary Fig. S1). During this time interval, subsurface (200–400 m depth) ocean annual mean temperatures range between 2 and 4°C. The presence of relatively warm and saline subsurface Atlantic water at the western and north-western Barents Sea margins during the LGM has been detected in sediment cores (Chauhan et al., 2014, 2016), suggesting mean summer SST values between 1 and 3°C (Nørgaard-Pedersen et al., 2003; Pflaumann et al., 2003). However, these values might be overestimated up to 3°C, due to well-known biases in the methodology used to reconstruct the SSTs from the paleoenvironmental proxies (Sarnthein et al., 2003). Therefore, we cannot exclude an overestimation of the western Barents Sea subsurface ocean forcing prescribed between 21 and 18 ky BP. We also highlight that the relatively simple sub-shelf melting parametrisation used in this study, accounting for ice-ocean heat exchanges only, could potentially amplify the effect of such an overestimation. The ocean temperature profiles prescribed at the western Barents Sea between 21 and 18 ky BP present a relatively warm subsurface layer (200–400 m depth) and sub-zero temperatures below 400 m depth (Supplementary Fig. S1). The LGM bedrock elevation in Bjørnøyrenna is mostly deeper than 400 m (Fig. 1), implying that sub-shelf melting rates will be systematically lower close to the grounding-line and higher towards the shelf edge. This is in contradiction with sub-shelf melting rates calculated over the Antarctic ice shelves with more refined methods such as ocean cavity circulation and plume models (Lazeroms et al., 2018; Reese et al., 2018; Pelle et al., 2019). In these studies, higher melt rates are simulated close to the grounding-line, and lower values,

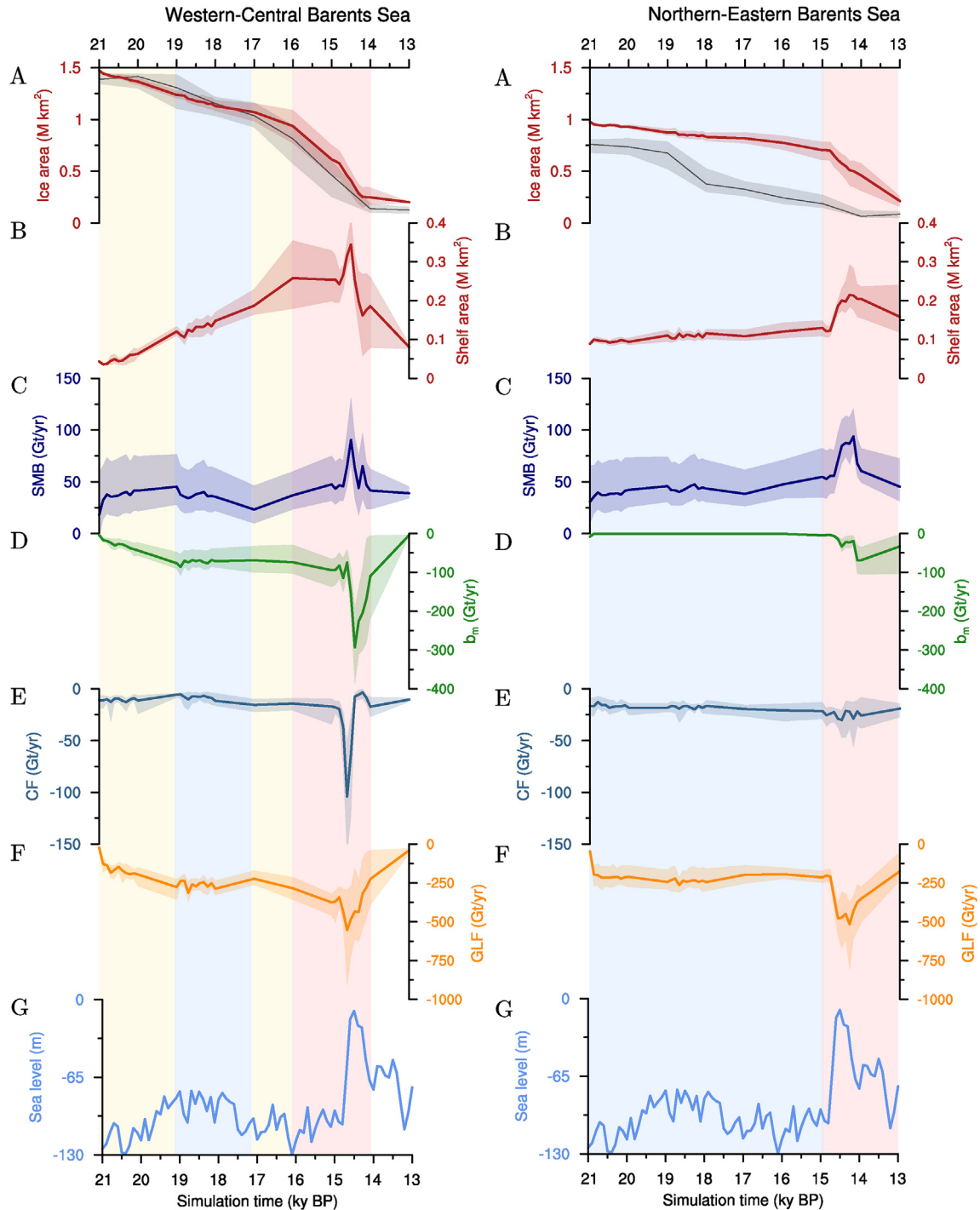


Fig. 8. Left panel: time series of integrated (a) ice area, (b) ice shelf area, (c) SMB, (d) sub-shelf melting, (e) calving flux, (f) grounding-line flux for the western and central Barents Sea in the minimum, maximum (shading) and average (solid lines) simulated scenario (see [Subsection 3.6](#)). Right panel: same values as in the left panel are shown for the northern and eastern Barents Sea. In both panels, the eustatic sea level prescribed in all the simulations of the ensemble is shown in (f).

possibly negative, are found as the distance from the grounding-line increases, due to the cooling effect of buoyant melt-water plumes rising along the shelf base towards the calving front. However, after 18 ky BP the ocean temperature profiles used to force the sub-shelf melting formulation show lower temperatures in the first 400 m and higher temperatures below ([Supplementary Fig. S1](#)). These types of ocean profiles are more similar to those used in ([Favier et al., 2019](#)) to assess the good agreement of the sub-shelf melting formulation used in this study with coupled ocean-ice

sheet simulations under idealised ocean warming scenarios. Therefore, we expect that the overestimation of sub-shelf melting rates away from the grounding-line did not occur after 18 ky BP, and more realistic sub-shelf melting patterns were simulated.

4.2.2. Late retreat of the eastern margin

Between 21 and 19 ky BP, the north-eastern and eastern margins of the ice sheet remain mostly unchanged in both the simulated and DATED-1 scenarios ([Fig. 10](#)). However, between 19 and 18 ky BP,

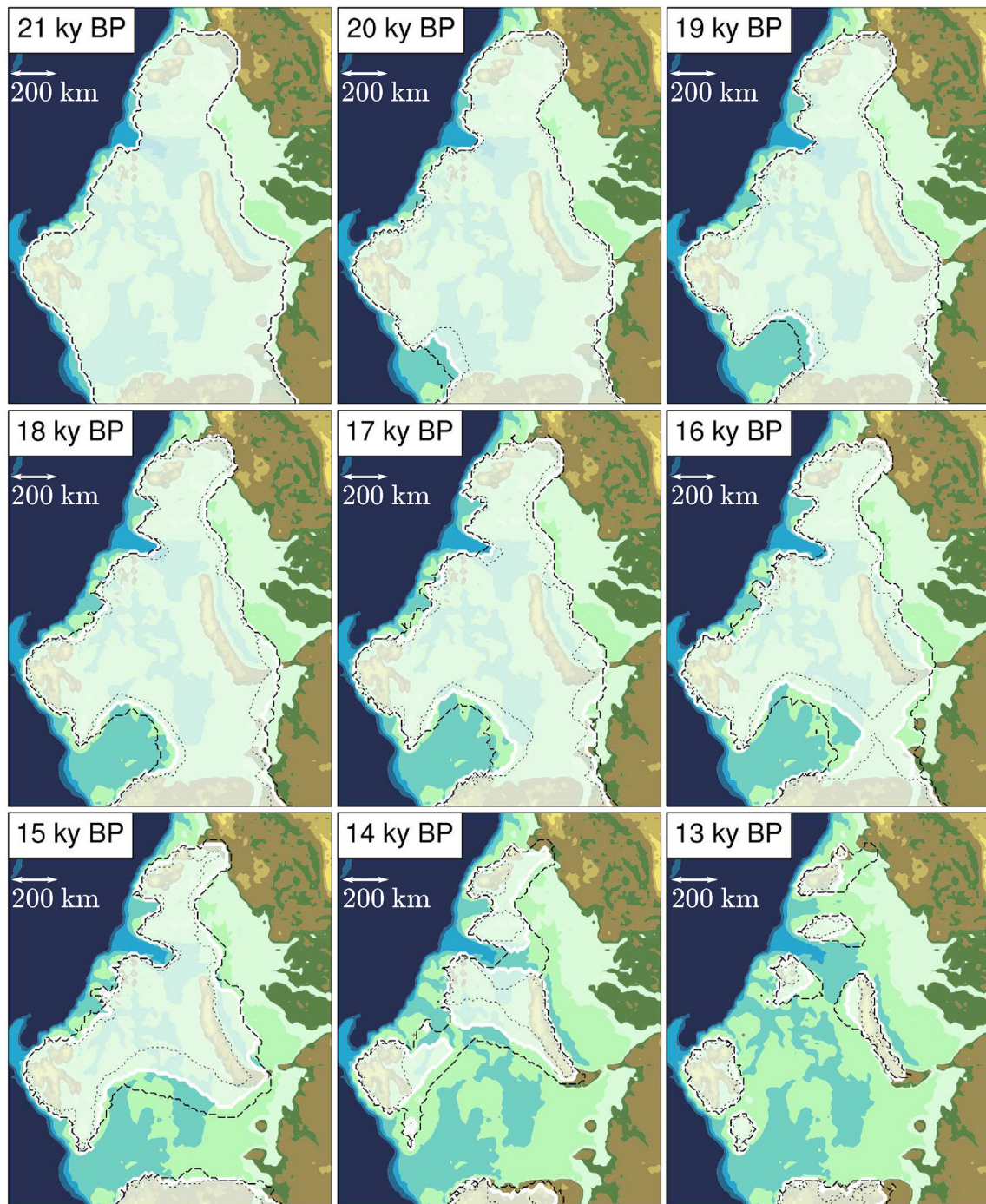


Fig. 9. Evolution of the simulated BSIS at 1000 yr time-slices between 21 and 13 ky BP. White solid, black dashed and black dotted lines represent most-credible, maximum and minimum simulated scenarios, respectively. The simulated ice sheet extent in the most-credible scenario is also white filled. PI topography is showed in the background as a reference, with the same color legend as in Fig. 6c. (For interpretation of the references to color in this figure legend, the reader is referred to the Web version of this article.)

the DATED-1 reconstruction suggests an abrupt retreat of the eastern ice sheet margin, reaching west of Novaya Zemlya towards the central Barents Sea. This retreat in the DATED-1 reconstruction continues, although at lower rates, in the following two thousand years, leaving St. Anna Trough ice-free by 17 ky BP and presenting at 16 ky BP an eastern margin well established in the central Barents Sea (Fig. 10). In all the simulated scenarios (min-avg-max) the eastern and north-eastern ice sheet margins show a drastically different behaviour, with the margin position not showing

significant changes between 21 and 15 ky BP (Figs. 9 and 10). This leads to an increase in the overestimated ice area up to 0.6 Mkm² (25–35% of the total area, Fig. 10 and Table 4).

The stable behaviour of the simulated eastern margin can be explained by looking at the atmospheric and oceanic conditions. First, the annual and July mean temperatures over Siberia and Kara Sea remains nearly constant at their LGM value until around 17 ky BP, and are still close to this value at 16 ky BP (Fig. 3A). Moreover, the ocean water still does not have access to the simulated eastern

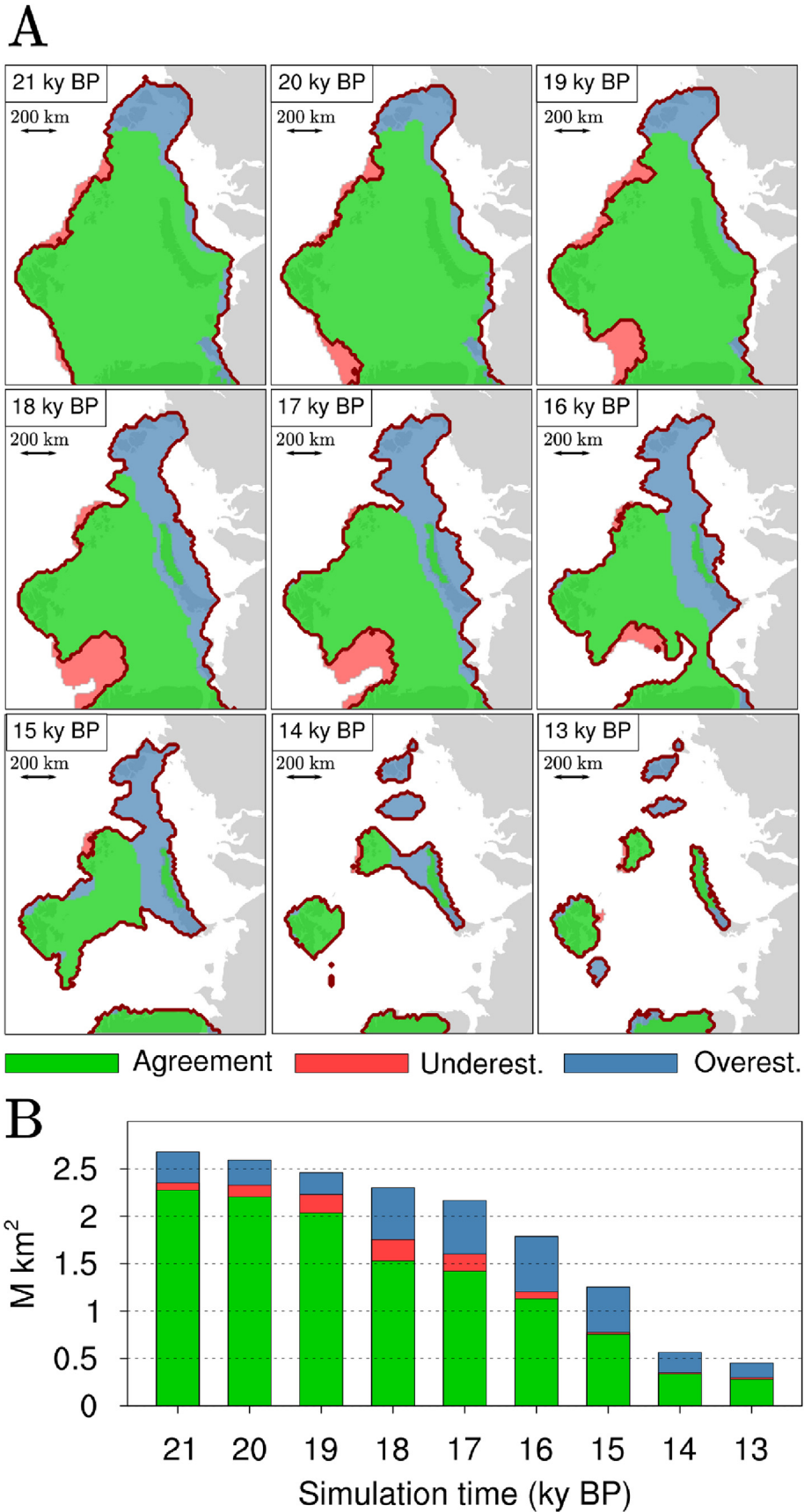


Fig. 10. (A) Time-slice evolution of the model-data agreement between the min-max-avg simulated scenarios and the DATED-1 min-max-mc reconstruction between 21 and 13 ky BP, shown every 1000 years. The green area indicates region where there is model-data agreement, whereas red and blue areas indicate regions of model-data underestimation and overestimation, respectively (see [Subsection 3.6](#)). (B) Model-data agreement, underestimation and overestimation total area at each time slice shown in (A) and with the same color legend. (For interpretation of the references to color in this figure legend, the reader is referred to the Web version of this article.)

and north-eastern ice sheet margins at 16 ky BP, as the north-eastern ice lobe is still grounded on the coast of Taymir Peninsula (Fig. 9). However, even if the connection with the Arctic ocean was open, the TraCE21ka Arctic Ocean temperature profile shows temperatures lower than -1°C throughout the water column until 16 ky BP (Supplementary Fig. S1), and the corresponding thermal forcing remains very close to zero until that time (Fig. 3B).

Proxies for summer SST and perennial sea ice cover (Nørgaard-Pedersen et al., 2003; Pflaumann et al., 2003; De Vernal et al., 2005) suggest that unlikely relatively warm subsurface Atlantic water could extend up to the easternmost part of the northern margin and trigger a large, sustained margin retreat as those suggested in the DATED-1 reconstruction. Moreover, even if this was the case, the subsurface Atlantic water would have also fringed the western and the westernmost part of the northern margin, thus triggering margin retreats at least comparable to those occurring at the eastern margin. This is not the case in the DATED-1 reconstruction, where the eastern ice sheet margin starts to retreat earlier than the western and northern margins. Even though the cold bias in the prescribed LGM climatology at the north-eastern and eastern margins of the ice sheet (see Subsection 4.1) could be a cause for the model/data mismatch, we find arguable that an increase in SMB alone due to regional warming would be capable of driving such a rapid ice sheet retreat. In view of this, we find unlikely that the model/data mismatch at the eastern ice sheet margin was entirely caused by bias in the climate forcings. A recent study combining a variety of marine proxies suggested that a combination of glacio-isostatic depression and high relative sea level initiated the last deglaciation of a marine-based sector of the BIIS, in absence of ocean warming and when eustatic sea level was at the LGM minimum (Cofaigh et al., 2019). A similar process could explain both the early retreat of the eastern ice sheet margin and the model/data mismatch, as this study only accounts for variations in eustatic sea level. Finally, it is highlighted that the glacial evolution of the eastern ice sheet margin remains poorly understood due to the limited amount of in-situ data available, as largely discussed in (Hughes et al., 2016), and the DATED-1 margin positions in the vicinity of Novaya Zemlya during and after the LGM are highly uncertain. It cannot be therefore excluded that the model-data mismatch observed in this region might be overestimated, and a relatively slow, steady retreat took place at the eastern margin of the ice sheet between 19 and 16 ky BP.

4.2.3. Collapse of the BSIS-SIS junction in the central Barents Sea

After the slowdown in ice retreat between 19 and 17 ky BP, the rate of ice area loss increase again, reaching $180\text{ km}^2/\text{yr}$ at 16 ky BP and leading to an ice area loss of 0.17 Mkm^2 between 17 and 16 ky BP (Fig. 7 and Table 3). In the following thousand years, the rate of ice area loss peaks to $390\text{ km}^2/\text{yr}$, the higher values registered since the beginning of the deglaciation, and the ice sheet lose 0.4 Mkm^2 of ice cover (Fig. 7 and Table 3). The area loss during this time interval is mainly occurring in the central Barents Sea (Fig. 8 and Table 3), which by 15 ky BP remains largely ice-free after the disconnection between the BSIS and the SIS in the average and maximum simulated scenarios (Fig. 9). In the minimum simulated scenario, the connection between the BSIS and the SIS is already relatively thin at 17 ky BP, and by 16 ky BP the ice sheets are already disconnected (Fig. 9). The southern branch of Bjørnøyrenna ice stream is deglaciated at 15 ky BP in all the simulated scenarios, whereas the northern branch of the ice stream occupies the inner part of Persey Trough in the northern Barents Sea both in the average and maximum simulated scenarios (Fig. 10). The area loss at the northern margin between 17 and 15 ky BP remains lower than 0.1 Mkm^2 , with an average retreat rate of $25\text{ km}^2/\text{yr}$ (Fig. 8 and Table 3).

Once again, the simulated retreat of the western ice sheet margin appears to be primarily driven by the prescribed ocean conditions rather than by SMB or sea level rise. In fact, during this time interval the integrated SMB remains positive and the prescribed sea level remains nearly constant, whereas the ice loss due to sub-shelf melting increase to 95 Gt/yr (Fig. 8 and Table 3). The increment of ice loss due to sub-shelf melting is caused by a relatively low increase in the ocean thermal forcing prescribed at the western Barents Sea margin below 200 m depth (Fig. 3A) due to the slow, gradual AMOC recovery in the TraCE21ka simulation between 17 and 15 ky BP, triggered by reduced Northern Hemisphere freshwater fluxes (Liu et al., 2009). Even though the decrease in sedimentary Pa/Th ratio (a proxy for AMOC strength) in a sediment core from Barbados seems to support this hypothesis (McManus et al., 2004), a more recent analysis of the Pa/Th ratio in a compilation of sediment cores from the Atlantic Ocean suggests that the AMOC was still weak until around 15 ky BP (Ng et al., 2018). However, the simulated AMOC in the TraCE21ka simulation is also weak between 17 and 15 ky BP and, despite its gradual increase during this time interval, the maximum AMOC transport does not exceed 5 Sv (Liu et al., 2009). Even though Pa/Th ratio represents a good proxy for ocean circulation, it cannot reliably quantify rates of AMOC weakening (Ivanovic et al., 2018). Therefore, it remains difficult to conclude whether the ocean thermal forcing prescribed at the western Barents Sea between 17 and 15 ky BP is overestimated.

The simulated and DATED-1 scenarios are in good agreement on the timing of the disintegration of the junction between the BSIS and the SIS, occurring between 17 and 16 ky BP in the minimum simulated and reconstructed scenario and between 16 and 15 ky BP in the simulated average and maximum scenarios and in the most-credible and maximum DATED-1 reconstructions (Hughes et al., 2016) (Fig. 9). In both reconstructed and simulated scenario, by 15 ky BP the southern margin of the BSIS has retreated north in the central Barents Sea, and the ice sheet presents a continuous ice cover from Svalbard in the north-west to Franz Josef Land (DATED-1 scenario) and Novaya and Severnaya Zemlya (simulated scenario) in the north-east (see for instance Fig. 10).

4.2.4. Final ice sheet deglaciation in the Barents and Kara seas

Between 15 and 14 ky BP, the simulated ice sheet experiences a further increase in the rate of area loss ($690\text{ km}^2/\text{yr}$ at 14.4 ky BP), losing 0.59 Mkm^2 of ice cover (Fig. 7 and Table 3). This major simulated area loss is due to the final ice sheet deglaciation, with the Barents and Kara seas remaining largely ice-free at 13 ky BP in all three simulated scenarios (Fig. 10). All the major troughs at the northern ice sheet margin are already deglaciated at 14 ky BP in the minimum and average scenarios, with the exception of the inner part of St. Anna Trough (Fig. 10). However, by 13 ky BP all the troughs are ice-free independently on the selected scenario, and the Kara Sea is entirely ice-free in the average and minimum simulated scenario, whereas an interconnected marine-based ice body joining Severnaya Zemlya and the Taymir Peninsula is still present in the maximum scenario (Fig. 10).

The ice sheet retreat between 15 and 14 ky BP is driven by a combination of sub-shelf melting and abrupt sea level rise prescribed between 14.6 and 14.4 ky BP (Figs. 7 and 8). In fact, during this time interval the ocean thermal forcing below 200 m keeps increasing in the Barents Sea and also starts to increase in the Arctic Ocean (Fig. 3A), due to the abrupt AMOC overshoot (i.e., recovery past its LGM level) during the Bølling-Allerød event simulated in TraCE21ka (Liu et al., 2009) (Fig. 3B). The sharp decrease in the Pa/Th ratio in sediment cores from Barbados and the Atlantic Ocean seems to support the relatively high AMOC export simulated in TraCE21ka during this short-lived event (McManus et al., 2004; Ng

Table 4
Simulated/DATED-1 ice sheet area agreement, overestimation and underestimation between the group of “admissible simulations” and the DATED-1 reconstruction throughout the deglaciation. Values are expressed both in Mkm² and as a percentage of the total ice sheet area $A_{TOT} = (A_S \cap A_D) \cup (A_S \setminus A_D) \cup (A_D \setminus A_S)$, where A_S is the simulated area and A_D is the DATED-1 area.

Simulation Time	Model/DATED-1 Agreement	Model/DATED-1 Overestimation	Model/DATED-1 Underestimation
21 ky BP	2.3 Mkm ² (85%)	0.3 Mkm ² (12%)	0.1 Mkm ² (3%)
20 ky BP	2.2 Mkm ² (85%)	0.3 Mkm ² (10%)	0.1 Mkm ² (5%)
19 ky BP	2.0 Mkm ² (83%)	0.2 Mkm ² (9%)	0.2 Mkm ² (8%)
18 ky BP	1.5 Mkm ² (66%)	0.5 Mkm ² (24%)	0.2 Mkm ² (10%)
17 ky BP	1.4 Mkm ² (66%)	0.6 Mkm ² (26%)	0.2 Mkm ² (8%)
16 ky BP	1.1 Mkm ² (63%)	0.6 Mkm ² (33%)	0.1 Mkm ² (4%)
15 ky BP	0.8 Mkm ² (60%)	0.5 Mkm ² (38%)	< 0.1 Mkm ² (2%)
14 ky BP	0.3 Mkm ² (60%)	0.2 Mkm ² (38%)	< 0.1 Mkm ² (2%)
13 ky BP	0.3 Mkm ² (62%)	0.2 Mkm ² (34%)	< 0.1 Mkm ² (4%)

et al., 2018), with relatively warm, saline Atlantic water reaching for the first time the Arctic ocean at the northern margin of the Eurasian basin (Supplementary Fig. S1). The abrupt, short-lived jump in prescribed sea level rise causes a rapid increase in the ice shelf area that, in combination with the ocean forcing, leads to peaks in ice loss due to sub-shelf melting around 450 Gt/yr and 255 Gt/yr at the southern and northern ice sheet margins, respectively (Fig. 8 and Table 3). After 14 ky BP, the prescribed sea level drops, but the sub-shelf melting remains negative, in spite of its decrease due to the reduction in ice shelf area, and leads to the final ice sheet collapse in the northern Barents Sea (Fig. 8 and Table 3). It is interesting to note how during the Bølling-Allerød event the SMB not only does not become negative, but also increases. In fact, by the onset of Bølling-Allerød the ice sheet has already retreated sufficiently north in the Barents Sea (Fig. 8), where the PI July mean air temperatures simulated with the IPSL-CM5A-LR AOGCM (Braconnot et al., 2012) are below zero (Fig. 2). The combination of sub-zero summer temperatures and increased snowfall (Fig. 3A) results in the SMB increase between 15 and 14 ky BP.

The simulated scenario is in agreement with the DATED-1 reconstruction on the timing of the deglaciation in the northern Barents Sea, remaining mostly ice-free at 13 ky BP (Fig. 10). By this time, both the simulated and DATED-1 scenarios show isolated ice cover above sea level in Svalbard, Franz Josef Land and Novaya Zemlya, whereas emerged lands in Severnaya Zemlya and south of Storfjordren Trough are ice-covered in the simulated scenarios only (Fig. 10).

4.3. Drivers of ice retreat and insights on the long-term stability of the WAIS

Overall, the simulated deglacial evolution of the BSIS presents a clear south-west to north-east deglaciation pattern (Figs. 8, 9 and 11) which reflects well the differences in the TraCE21ka ocean forcing prescribed at the western and northern ice sheet margins. Even though changes in eustatic sea level do affect the grounding-line position, the magnitude of their impact appears largely dependent on the oceanic background. This is clearly shown by the simulated ice retreat at the northern ice sheet margin until 15 ky BP, where in absence of sub-shelf melting rates of sea level rise and area loss are up to 5 times lower than at the western margin (Table 3). Also the different magnitude and timing of the peaks in sub-shelf melting at the western and northern margins in response to the 14.6–14.4 ky BP abrupt eustatic sea level rise indicate that changes in eustatic sea level amplified the effects of ocean warming, rather than driving the ice retreat (Fig. 8 and Table 3). Considering that the SMB remains positive throughout the deglaciation (Fig. 8) we can identify the ocean forcing as the primary driver of the simulated last deglaciation of the BSIS. The strong impact of sub-shelf melting on the evolution of marine-based ice

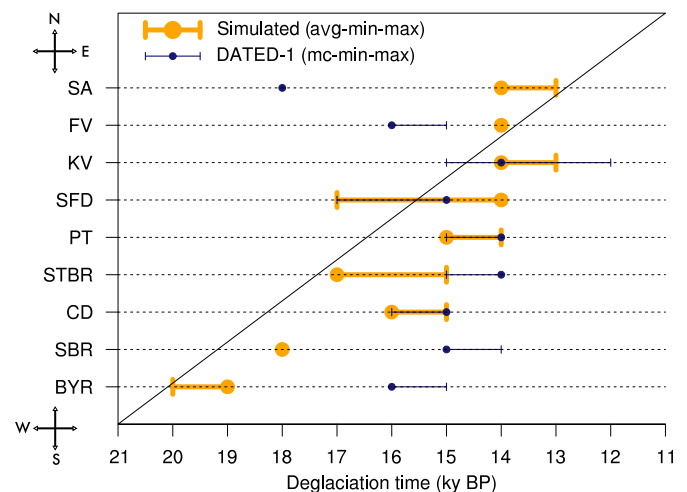


Fig. 11. Simulated (orange dots and lines) and DATED-1 (dark blue dots and lines) deglaciation timing for the individual ice streams shown in Fig. 1. Dots represent the deglaciation timing in the average simulated scenario and DATED-1 most-credible reconstruction, whereas lines indicate the deglaciation timing in the minimum and maximum simulated and DATED-1 scenarios. As shown by the black arrow, the ice streams are ordered on the y-axis from south-west (SW) to north-east (NE). BYR = Bjørnøyrenna, SBR = Sentralbankrenna, CD = Central Deep, STBR = Storbankrenna, PT = Persey Trough, SFD = Storfjordrenna, KV = Kvitøya Trough, FV = Franz Victoria Trough, SA = St. Anna Trough. (For interpretation of the references to color in this figure legend, the reader is referred to the Web version of this article.)

sheets on multi-millennial timescales, as opposed to the minor role played by atmospheric forcing and sea level rise, has also been demonstrated in recent ice sheet modelling studies focusing on the Eurasian ice sheets (Alvarez-Solas et al., 2019) and on the Antarctic Ice Sheet (Mackintosh et al., 2011; Lowry et al., 2019; Blasco et al., 2019).

In addition, our results highlight that the sub-shelf melting has a very strong control on the simulated grounding-line discharge. At the northern ice sheet margin, the grounding-line flux curve remains nearly flat, with minor oscillations due to changes in the eustatic sea level, until the sub-shelf melting starts to increase after 15 ky BP (Fig. 8). In contrast, the alternation of increasing/decreasing trends in sub-shelf melting at the western ice sheet margin corresponds to intervals of increasing/decreasing grounding-line discharge (Fig. 8). We focus in particular on the interval 17–15 ky BP, which is marked by the collapse of the junction between the BSIS and the SIS in the central Barents Sea. During this time interval, the eustatic sea level is relatively stable (Fig. 8) and the ocean thermal forcing below 200 m slowly, gradually increase from around 5 to 20°C² (Fig. 3B), which corresponds to an increase in ocean temperatures above freezing of around +2.3°C in two thousand years (around 0.1°C per century). This prescribed ocean

warming causes a 35% increase in sub-shelf melting (+25 Gt/yr), which results in turn in a 65% increase in grounding-line discharge (+150 Gt/yr) and a nearly doubled rate of sea level rise from 0.56 to 1.04 mm/yr (Fig. 8 and Table 3). This shows that a prolonged, gradual ocean warming is capable of triggering sustained grounded ice discharge over multi-millennial timescales, even without including positive feedbacks such as MISI, acknowledged to play a role at least as important as the oceanic forcing in Antarctica (Joughin et al., 2014; Rignot et al., 2014; Jenkins et al., 2018), and MICI. Recent observations showed significant ocean warming over the last decades in the Bellingshausen and Amundsen shelves in West Antarctica, at trends of 0.1–0.3°C per decade (Schmidt et al., 2014). These trends of ocean warming are at least one order of magnitude larger than those driving the collapse of the BSIS-SIS junction in the central Barents Sea between 17 and 15 ky BP. This suggests that if current trends will continue, the long-term stability of the Bellingshausen and Amundsen sectors in West Antarctica could be already at stake within the next centuries.

Finally, it is remarked that a similar south-west to north-east deglaciation pattern has also recently been obtained with a first-order ice sheet model (Patton et al., 2017). It is stressed that our study differs fundamentally from (Patton et al., 2017) because of methodological differences in the treatment of climatic and oceanic forcing as drivers of the ice sheet simulations. In fact, reference climatology and associated climate forcings in (Patton et al., 2017) have been regionally tuned in order to match a suite of empirical data, and the retreat of the marine-terminating ice sheet margins is regulated by an empirical function relating calving to ice thickness and water depth. In this study, we focused instead on providing a simulated scenario of the last deglaciation of the BSIS reflecting the original climatic and oceanic forcings. For this reason, a more meaningful direct comparison between the two studies is not possible.

5. Conclusions

A perturbed physics ensemble of transient ice sheet model simulations has been performed to investigate the evolution of the BSIS during the last deglaciation. The simulations are forced with transient macro-regional atmospheric and oceanic conditions and a transient eustatic sea level curve. The ensemble of transient simulations has been validated against the DATED-1 reconstruction to construct average, minimum and maximum deglaciation scenarios. The simulated deglaciation scenarios have been then analyzed and compared with the DATED-1 reconstruction (Hughes et al., 2016), providing the following insights:

- The simulated deglaciation starts immediately after the LGM, with a rapid retreat of the western ice sheet margin into the central Barents Sea between 21 and 18 ky BP. This simulated retreat is primarily driven by the ocean forcing prescribed at the western ice sheet margin, with the initial eustatic sea level rise amplifying the ice sheet sensitivity to sub-shelf melting. The initial simulated retreat of the western ice sheet margin is not supported by the DATED-1 reconstruction, suggesting that the western margin remained stable until 19 ky BP. This mismatch can be explained either by an excessive model sensitivity to sub-shelf melting, or by an overestimation of the subsurface Atlantic water temperature in the TraCE21ka simulation, likely amplified by the relatively simple sub-shelf melting parametrisation used in this study.
- The simulated eastern ice sheet margin remains extremely stable until 15 ky BP, due to the cold atmospheric and oceanic conditions prescribed over this area. This is in clear contradiction with the DATED-1 reconstruction, suggesting a very rapid

retreat of this margin between 19 and 18 ky BP. A first consideration to explain the model/data mismatch is that our simulations do not account for variations in relative sea level, which might have triggered the initial eastern margin retreat in spite of the cold climatic conditions. However, we also note that the eastern margin position throughout the deglaciation is highly uncertain in the DATED-1 reconstruction (Hughes et al., 2016). It cannot be therefore excluded that the model-data mismatch observed in this region might be overestimated and the eastern margin experienced a slower, steady retreat during this time interval.

- The disintegration of the connection between the SIS and the BSIS in the central Barents Sea occurs between 16 and 15 ky BP in the simulated average and maximum scenarios, whereas the minimum simulated scenario suggests instead that this event occurred earlier between 17 and 16 ky BP. The simulated scenarios are in good agreement with the DATED-1 scenarios for the timing of this event, placed between 16 and 15 ky BP in the most-credible and minimum reconstructions and between 17 and 16 ky BP in the maximum reconstruction. The collapse of the BSIS-SIS junction is driven by a slow, gradual increase in the prescribed Barents Sea ocean forcing below 200 m depth after 17 ky BP.
- The final simulated ice sheet collapse takes place between 15 and 13 ky BP, driven by the increase in the prescribed ocean forcing both in the Barents Sea and in the Arctic Ocean. The abrupt eustatic sea level rise prescribed between 14.6 and 14.4 ky BP contribute to accelerate the ice sheet collapse in the central Barents Sea and, to a less extent, in the northern Barents Sea. The simulated scenarios are in agreement with the DATED-1 reconstruction on the timing of the final ice sheet final collapse, with the exception of few ice remnants in the Kara Sea.
- Overall, the simulated deglacial evolution of the BSIS exhibits a clear south-west to north-east deglaciation pattern, primarily driven by the ocean forcing at the western and northern ice sheet margins. Prescribed eustatic sea level rise contributes to amplify the ice sheet sensitivity to sub-shelf melting over relatively short time intervals. The strong impact of sub-shelf melting on the retreat of marine-based ice sheets has also been recently demonstrated in ice sheet modelling studies focusing on the multi-millennial evolution of the Eurasian ice sheets (Alvarez-Solas et al., 2019) and the Antarctic Ice Sheet (Mackintosh et al., 2011; Lowry et al., 2019; Blasco et al., 2019).
- Our results highlight that the sub-shelf melting has a very strong control on the simulated grounding-line discharge. In particular, the collapse of the junction between the BSIS and the SIS in the central Barents Sea occurs in response to an increase in ocean temperatures above freezing of around +2.3 °C in two thousand years (around 0.1 °C per century). This prescribed ocean warming results in a 65% increase in grounding-line discharge and a nearly doubled rate of sea level rise, thus showing that a prolonged, gradual ocean warming is capable of triggering sustained grounded ice discharge over multi-millennial timescales, even without including positive feedbacks such as MISI and MICI.

Author contributions

Michele Petrini: Methodology, Software, Validation, Formal analysis, Investigation, Visualization, Writing - Original Draft. Florence Colleoni: Conceptualization, Supervision, Writing - Review & Editing. Nina Kirchner: Conceptualization, Supervision, Resources, Writing - Review & Editing. Anna LC Hughes: Funding acquisition, Resources, Writing - Review & Editing. Angelo

Camerlenghi: Conceptualization, Project administration, Funding acquisition, Writing – Review & Editing. Michele Rebesco: Conceptualization, Project Administration, Funding acquisition, Writing – Review & Editing. Renata G Lucchi: Conceptualization, Resources, Writing – Review & Editing. Emanuele Forte: Conceptualization, Project Administration, Writing – Review & Editing. Renato R Colucci: Conceptualization, Supervision, Writing – Review & Editing. Riko Noormets: Conceptualization, Writing – Review & Editing. Jan Mangerud: Writing – Review & Editing.

Declaration of competing interest

The authors declare that they have no known competing financial interests or personal relationships that could have appeared to influence the work reported in this paper.

Acknowledgements

The research reported in this work was supported by Oceanography and Applied Geophysics (OGS) and CINECA under HPC-TRES program award number 2016-03 and by the FORMAS grant 214-2013-1600 to NK. We acknowledge the CINECA award under the ISCR initiative, for the availability of high performance computing resources and support. Parts of the computations were performed on resources provided by the Swedish National Infrastructure for Computing (SNIC) at PDC Centre for High Performance Computing at KTH. MP was supported by a Bjercknes Visiting Fellowship from the Bjercknes Centre for Climate Research in July 2018. JM and ALCH acknowledge the strategic project RISES funded by the Bjercknes Centre for Climate Research, Norway. The authors would like to thank the anonymous reviewers for their valuable comments and suggestions to improve the quality of the paper.

Appendix A. Supplementary data

Supplementary data to this article can be found online at <https://doi.org/10.1016/j.quascirev.2020.106314>.

References

- Abe-Ouchi, A., Segawa, T., Saito, F., 2007. Climatic conditions for modelling the Northern Hemisphere ice sheets throughout the ice age cycle. *Clim. Past* 3 (3), 423–438.
- Alvarez-Solas, J., Banderas, R., Robinson, A., Montoya, M., 2019. Ocean-driven millennial-scale variability of the Eurasian ice sheet during the last glacial period simulated with a hybrid ice-sheet–shelf model. *Clim. Past* 15 (3), 957–979.
- Álvarez Solás, J., Montoya, M., Ritz, C., Ramstein, G., Charbit, S., Dumas, C., Nisancioglu, K., Dokken, T., Ganopolski, A., 2011. Heinrich event 1: an example of dynamical ice-sheet reaction to oceanic changes. *Clim. Past* 7 (4), 1297–1306.
- Andersen, E.S., Dokken, T.M., Elverhøi, A., Solheim, A., Fossen, I., 1996. Late Quaternary sedimentation and glacial history of the western Svalbard continental margin. *Mar. Geol.* 133 (3–4), 123–156.
- Andersen, K.K., Azuma, N., Barnola, J., Bigler, M., et al., 2004. High-resolution record of Northern Hemisphere climate extending into the last interglacial period. *Nature* 431 (7005), 147.
- Andreassen, K., Winsborrow, M., 2009. Signature of ice streaming in Bjørnøyrenna, polar north Atlantic, through the pleistocene and implications for ice-stream dynamics. *Ann. Glaciol.* 50 (52), 17–26.
- Applegate, P.J., Parizek, B.R., Nicholas, R.E., Alley, R.B., Keller, K., 2015. Increasing temperature forcing reduces the Greenland Ice Sheet's response time scale. *Clim. Dynam.* 45 (7–8), 2001–2011.
- Barthel, A., Agosta, C., Little, C.M., Hattermann, T., Jourdain, N.C., Goelzer, H., Nowicki, S., Seroussi, H., Straneo, F., Bracegirdle, T.J., 2019. CMIP5 Model Selection for ISMIP6 Ice Sheet Model Forcing: Greenland and Antarctica. Under review for the journal *The Cryosphere* (CT).
- Bartlein, P.J., Harrison, S., Brewer, S., Connor, S., Davis, B., Gajewski, K., Guiot, J., Harrison-Prentice, T., Henderson, A., Peyron, O., et al., 2011. Pollen-based continental climate reconstructions at 6 and 21 ka: a global synthesis. *Clim. Dynam.* 37 (3–4), 775–802.
- Bjarnadóttir, L.R., Winsborrow, M.C., Andreassen, K., 2014. Deglaciation of the central Barents Sea. *Quat. Sci. Rev.* 92, 208–226.
- Blasco, J., Tabone, I., Alvarez-Solas, J., Robinson, A., Montoya, M., 2019. The Antarctic Ice Sheet response to glacial millennial-scale variability. *Clim. Past* 15 (1), 121–133.
- Braconnot, P., Harrison, S.P., Kageyama, M., Bartlein, P.J., Masson-Delmotte, V., Abe-Ouchi, A., Otto-Bliesner, B., Zhao, Y., 2012. Evaluation of climate models using palaeoclimatic data. *Nat. Clim. Change* 2 (6), 417–424.
- Braithwaite, R.J., 1984. Calculation of degree-days for glacier-climate research. *Z. Gletscherkd. Glazialgeol.* 20, 1–8.
- Charbit, S., Ritz, C., Ramstein, G., 2002. Simulations of Northern Hemisphere ice-sheet retreat: sensitivity to physical mechanisms involved during the Last Deglaciation. *Quat. Sci. Rev.* 21 (1–3), 243–265.
- Chauhan, T., Rasmussen, T., Noormets, R., Jakobsson, M., Hogan, K., 2014. Glacial history and paleoceanography of the southern Yermak Plateau since 132 ka BP. *Quat. Sci. Rev.* 92, 155–169.
- Chauhan, T., Rasmussen, T.L., Noormets, R., 2016. Palaeoceanography of the Barents Sea continental margin, north of Nordaustlandet, Svalbard, during the last 74 ka. *Boreas* 45 (1), 76–99.
- Cofaigh, C.O., Weilbach, K., Lloyd, J.M., Benetti, S., Callard, S.L., Purcell, C., Chiverrell, R.C., Dunlop, P., Saher, M., Livingstone, S.J., et al., 2019. Early deglaciation of the British-Irish Ice Sheet on the Atlantic shelf northwest of Ireland driven by glacioisostatic depression and high relative sea level. *Quat. Sci. Rev.* 208, 76–96.
- Colleoni, F., De Santis, L., Siddoway, C.S., Bergamasco, A., Golledge, N.R., Lohmann, G., Passchier, S., Siegert, M.J., 2018. Publisher Correction: spatio-temporal variability of processes across Antarctic ice-bed–ocean interfaces. *Nat. Commun.* 9 (1), 2742.
- Colleoni, F., Quiquet, A., Masina, S., 2016. Long-term Safety of a Planned Geological Repository for Spent Nuclear Fuel in Forsmark – Phase 2: Impact of Ice Sheet Dynamics, Climate Forcing and Multi-Variate Sensitivity Analysis on Maximum Ice Sheet Thickness. Swedish Nuclear Fuel and Waste Management Co, Stockholm, Sweden. Technical Report SKB TR-14-21.
- Cook, A., Holland, P., Meredith, M., Murray, T., Luckman, A., Vaughan, D., 2016. Ocean forcing of glacier retreat in the western Antarctic Peninsula. *Science* 353 (6296), 283–286.
- De Vernal, A., Eynaud, F., Henry, M., Hillaire-Marcel, C., Londeix, L., Mangin, S., Matthiessen, J., Marret, F., Radi, T., Rochon, A., et al., 2005. Reconstruction of sea-surface conditions at middle to high latitudes of the Northern Hemisphere during the Last Glacial Maximum (LGM) based on dinoflagellate cyst assemblages. *Quat. Sci. Rev.* 24 (7–9), 897–924.
- DeConto, R.M., Pollard, D., 2016. Contribution of Antarctica to past and future sea-level rise. *Nature* 531 (7596), 591.
- Dowdeswell, J.A., Hogan, K., Evans, J., Noormets, R., Ó Cofaigh, C., Ottesen, D., 2010. Past ice-sheet flow east of Svalbard inferred from streamlined subglacial landforms. *Geology* 38 (2), 163–166.
- Dowdeswell, J.A., Siegert, M.J., 1999. Ice-sheet numerical modeling and marine geophysical measurements of glacier-derived sedimentation on the Eurasian Arctic continental margins. *Geol. Soc. Am. Bull.* 111 (7), 1080–1097.
- Dumas, C., 2002. Modélisation de l'évolution de l'Antarctique depuis le dernier cycle glaciaire-interglaciaire jusqu'au futur: importance relative des différents processus physiques et rôle des données d'entrée. Ph.D. thesis. Université Joseph-Fourier-Grenoble I.
- Edwards, T.L., Brandon, M.A., Durand, G., Edwards, N.R., Golledge, N.R., Holden, P.B., Nias, I.J., Payne, A.J., Ritz, C., Wernecke, A., 2019. Revisiting Antarctic ice loss due to marine ice-cliff instability. *Nature* 566 (7742), 58.
- Estevés, M., Bjarnadóttir, L.R., Winsborrow, M.C., Shackleton, C.S., Andreassen, K., 2017. Retreat patterns and dynamics of the Svalbard Bank glacial system, central Barents Sea. *Quat. Sci. Rev.* 169, 131–147.
- Fausto, R.S., Ahlstrøm, A.P., Van As, D., Bøggild, C.E., Johnsen, S.J., 2009. A new present-day temperature parameterization for Greenland. *J. Glaciol.* 55 (189), 95–105.
- Fausto, R.S., Ahlstrøm, A.P., Van As, D., Steffen, K., 2011. Present-day temperature standard deviation parameterization for Greenland. *J. Glaciol.* 57 (206), 1181–1183.
- Favier, L., Durand, G., Cornford, S.L., Gudmundsson, G.H., Gagliardini, O., Gillet-Chaulet, F., Zwinger, T., Payne, A., Le Brocq, A.M., 2014. Retreat of Pine Island Glacier controlled by marine ice-sheet instability. *Nat. Clim. Change* 4 (2), 117.
- Favier, L., Jourdain, N.C., Jenkins, A., Merino, N., Durand, G., Gagliardini, O., Gillet-Chaulet, F., Mathiot, P., 2019. Assessment of sub-shelf melting parameterizations using the Ocean-ice sheet coupled model NEMO(v3.6)-Elmer/Ice(v8.3). *Geosci. Model Dev. Discuss. (GMDD)* 2019, 1–40. <https://doi.org/10.5194/gmd-2019-26>. <https://www.geosci-model-dev-discuss.net/gmd-2019-26/>.
- Fransner, O., Noormets, R., Chauhan, T., Ó Cofaigh, C., Regan, M., Jakobsson, M., 2018. Late Weichselian ice stream configuration and dynamics in Albertini Trough, northern Svalbard margin. *arXiv* 1804.01111.
- Fransner, O., Noormets, R., Flink, A., Hogan, K., O'Regan, M., Jakobsson, M., 2017. Glacial landforms and their implications for glacier dynamics in Rjippfjorden and Duvefjorden, northern Nordaustlandet, Svalbard. *J. Quat. Sci.* 32 (3), 437–455.
- Goelzer, H., Huybrechts, P., Loutre, M.F., Goosse, H., Fichetef, T., Mouchet, A., 2011. Impact of Greenland and Antarctic ice sheet interactions on climate sensitivity. *Clim. Dynam.* 37 (5–6), 1005–1018.
- Gregoire, L.J., Otto-Bliesner, B., Valdes, P.J., Ivanovic, R., 2016. Abrupt Bølling warming and ice saddle collapse contributions to the Meltwater Pulse 1a rapid sea level rise. *Geophys. Res. Lett.* 43 (17), 9130–9137.
- Greve, R., 2005. Relation of measured basal temperatures and the spatial distribution of the geothermal heat flux for the Greenland ice sheet. *Ann. Glaciol.* 42,

- 424–432.
- Greve, R., Saito, F., Abe-Ouchi, A., 2011. Initial results of the SeaRISE numerical experiments with the models SICOPOLIS and ICES for the Greenland ice sheet. *Ann. Glaciol.* 52 (58), 23–30.
- Gudmundsson, H., Krug, J., Durand, G., Favier, L., Gagliardini, O., 2012. The stability of grounding lines on retrograde slopes. *Cryosphere* 6 (6), 1497–1505.
- Hogan, K., Dowdeswell, J., Noormets, R., Evans, J., Cofaigh, C.Ó., Jakobsson, M., 2010a. Submarine landforms and ice-sheet flow in the Kvitøya Trough, northwestern Barents Sea. *Quat. Sci. Rev.* 29 (25–26), 3545–3562.
- Hogan, K., Dowdeswell, J., Noormets, R., Evans, J., Cofaigh, C.Ó., 2010b. Evidence for full-glacial flow and retreat of the late Weichselian ice sheet from the waters around Kong Karls land, eastern Svalbard. *Quat. Sci. Rev.* 29 (25–26), 3563–3582.
- Holland, P.R., Jenkins, A., Holland, D.M., 2008. The response of ice shelf basal melting to variations in ocean temperature. *J. Clim.* 21 (11), 2558–2572.
- Hughes, A.L., Gyllencreutz, R., Lohne, Ø.S., Mangerud, J., Svendsen, J.I., 2016. The last Eurasian ice sheets—a chronological database and time-slice reconstruction, DATED-1. *Boreas* 45 (1), 1–45.
- Hütter, K., 1983. *Theoretical Glaciology: Material Science of Ice and the Mechanics of Glacier and Ice Sheets*. D Reidel, Norwell, Mass, p. 510.
- Ivanovic, R., Gregoire, L., Burke, A., Wickert, A., Valdes, P., Ng, H., Robinson, L., McManus, J., Mitrovica, J., Lee, L., et al., 2018. Acceleration of northern ice sheet melt induces AMOC slowdown and northern cooling in simulations of the early last deglaciation. *Paleoceanogr. Paleoclimatol.* 33 (7), 807–824.
- Jakobsson, M., 2014. *International Bathymetric Chart of the Arctic Ocean (IBCAO)*. Springer.
- Jenkins, A., Shoosmith, D., Dutrieux, P., Jacobs, S., Kim, T.W., Lee, S.H., Ha, H.K., Stammerjohn, S., 2018. West Antarctic ice sheet retreat in the Amundsen sea driven by decadal oceanic variability. *Nat. Geosci.* 11 (10), 733–738.
- Joughin, I., Smith, B.E., Medley, B., 2014. Marine ice sheet collapse potentially under way for the Thwaites Glacier Basin, West Antarctica. *Science* 344 (6185), 735–738.
- Khazendar, A., Rignot, E., Schroeder, D.M., Seroussi, H., Schodlok, M.P., Scheuchl, B., Mouginot, J., Sutterley, T.C., Velicogna, I., 2016. Rapid submarine ice melting in the grounding zones of ice shelves in West Antarctica. *Nat. Commun.* 7, 13243.
- Kirchner, N., Hutter, K., Jakobsson, M., Gyllencreutz, R., 2011. Capabilities and limitations of numerical ice sheet models: a discussion for Earth-scientists and modelers. *Quat. Sci. Rev.* 30 (25–26), 3691–3704.
- Kleiber, H., Knies, J., Niessen, F., 2000. The late Weichselian glaciation of the Franz Victoria Trough, northern Barents Sea: ice sheet extent and timing. *Mar. Geol.* 168 (1–4), 25–44.
- Landvik, J.Y., Bondevik, S., Elverhøi, A., Fjeldskaar, W., Mangerud, J., Salvigsen, O., Siegert, M.J., Svendsen, J.I., Vorren, T.O., 1998. The last glacial maximum of Svalbard and the Barents Sea area: ice sheet extent and configuration. *Quat. Sci. Rev.* 17 (1), 43–75.
- Laske, G., 1997. A global digital map of sediment thickness. *Eos Trans AGU* 78, F483.
- Lazeroms, W.M., Jenkins, A., Gudmundsson, G.H., Van De Wal, R.S., 2018. Modelling present-day basal melt rates for Antarctic ice shelves using a parametrization of buoyant meltwater plumes. *Cryosphere* 12 (1), 49–70.
- Le Meur, E., Huybrechts, P., 1996. A comparison of different ways of dealing with isostasy: examples from modelling the Antarctic ice sheet during the last glacial cycle. *Ann. Glaciol.* 23, 309–317.
- Liu, Z., Otto-Bliessner, B., He, F., Brady, E., Tomas, R., Clark, P., Carlson, A., Lynch-Stieglitz, J., Curry, W., Brook, E., et al., 2009. Transient simulation of last deglaciation with a new mechanism for Bølling-Allerød warming. *Science* 325 (5938), 310–314.
- Llopert, J., Urgeles, R., Camerlenghi, A., Lucchi, R.G., Rebesco, M., De Mol, B., 2015. Late quaternary development of the Storfjorden and Kveithola trough mouth fans, northwestern Barents Sea. *Quat. Sci. Rev.* 129, 68–84.
- Lowry, D.P., Gollledge, N.R., Bertler, N.A., Jones, R.S., McKay, R., 2019. Deglacial grounding-line retreat in the Ross Embayment, Antarctica, controlled by ocean and atmosphere forcing. *Sci. Adv.* 5 (8), eaav8754.
- Lucchi, R., Camerlenghi, A., Rebesco, M., Colmenero-Hidalgo, E., Sierro, F., Sagnotti, L., Urgeles, R., Melis, R., Morigi, C., Bárcena, M.A., et al., 2013. Post-glacial sedimentary processes on the Storfjorden and Kveithola trough mouth fans: significance of extreme glacial marine sedimentation. *Global Planet. Change* 111, 309–326.
- Ma, Y., Gagliardini, O., Ritz, C., Gillet-Chaulet, F., Durand, G., Montagnat, M., 2010. Enhancement factors for grounded ice and ice shelves inferred from an anisotropic ice-flow model. *J. Glaciol.* 56 (199), 805–812. <https://doi.org/10.3189/002214310794457209>, 8. <https://hal-insu.archives-ouvertes.fr/insu-00653459>.
- MacAyeal, D.R., 1989. Large-scale ice flow over a viscous basal sediment: theory and application to ice stream B, Antarctica. *J. Geophys. Res.: Solid Earth* 94 (B4), 4071–4087.
- Mackintosh, A., Gollledge, N., Domack, E., Dunbar, R., Leventer, A., White, D., Pollard, D., DeConto, R., Fink, D., Zwart, D., et al., 2011. Retreat of the East Antarctic ice sheet during the last glacial termination. *Nat. Geosci.* 4 (3), 195.
- Marshall, S.J., Sharp, M.J., Burgess, D.O., Anslow, F.S., 2007. Near-surface-temperature lapse rates on the Prince of Wales Icefield, Ellesmere Island, Canada: implications for regional downscaling of temperature. *Int. J. Climatol.: J. Roy. Meteorol. Soc.* 27 (3), 385–398.
- Marsiat, I., 1994. Simulation of the Northern Hemisphere continental ice sheets over the last glacial-interglacial cycle: experiments with a latitude-longitude vertically integrated ice sheet model coupled to a zonally averaged climate model. *Paleoclimates* 1 (1), 59–98.
- Martin, M., Winkelmann, R., Haseloff, M., Albrecht, T., Bueler, E., Khroulev, C., Levermann, A., 2011. The Potsdam parallel ice sheet model (PISM-PIK)—Part 2: dynamic equilibrium simulation of the Antarctic ice sheet. *Cryosphere* 5 (3), 727–740.
- McManus, J.F., Francois, R., Gherardi, J.M., Keigwin, L.D., Brown-Leger, S., 2004. Collapse and rapid resumption of Atlantic meridional circulation linked to deglacial climate changes. *Nature* 428 (6985), 834.
- Mercur, J.H., 1970. A former ice sheet in the Arctic Ocean? *Palaeogeogr. Palaeoclimatol. Palaeoecol.* 8 (1), 19–27.
- Morland, L., 1984. Thermomechanical balances of ice sheet flows. *Geophys. Astrophys. Fluid Dynam.* 29 (1–4), 237–266.
- Newton, A., Knutz, P., Huuse, M., Gannon, P., Brocklehurst, S., Clausen, O., Gong, Y., 2017. Ice stream reorganization and glacial retreat on the northwest Greenland shelf. *Geophys. Res. Lett.* 44 (15), 7826–7835.
- Ng, H.C., Robinson, L.F., McManus, J.F., Mohamed, K.J., Jacobel, A.W., Ivanovic, R.F., Gregoire, L.J., Chen, T., 2018. Coherent deglacial changes in western Atlantic Ocean circulation. *Nat. Commun.* 9 (1), 1–10.
- Nielsen, T., Rasmussen, T.L., 2018. Reconstruction of ice sheet retreat after the Last Glacial maximum in Storfjorden, southern Svalbard. *Mar. Geol.* 402, 228–243.
- Nørgaard-Pedersen, N., Spielhagen, R.F., Erlenkeuser, H., Grootes, P.M., Heinemeier, J., Knies, J., 2003. Arctic Ocean during the Last Glacial Maximum: Atlantic and polar domains of surface water mass distribution and ice cover. *Paleoceanogr. Paleoclimatol.* 18 (3).
- Ottesen, D., Dowdeswell, J., Rise, L., 2005. Submarine landforms and the reconstruction of fast-flowing ice streams within a large Quaternary ice sheet: the 2500-km-long Norwegian-Svalbard margin (57–80 N). *Geol. Soc. Am. Bull.* 117 (7–8), 1033–1050.
- Paolo, F.S., Fricker, H.A., Padman, L., 2015. Volume loss from Antarctic ice shelves is accelerating. *Science* 348 (6232), 327–331.
- Patton, H., Andreassen, K., Bjarnadóttir, L.R., Dowdeswell, J.A., Winsborrow, M.C., Noormets, R., Polyak, L., Auriac, A., Hubbard, A., 2015. Geophysical constraints on the dynamics and retreat of the Barents Sea ice sheet as a paleobenchmark for models of marine ice sheet deglaciation. *Rev. Geophys.* 53 (4), 1051–1098.
- Patton, H., Hubbard, A., Andreassen, K., Auriac, A., Whitehouse, P.L., Stroeven, A.P., Shackleton, C., Winsborrow, M., Heyman, J., Hall, A.M., 2017. Deglaciation of the Eurasian ice sheet complex. *Quat. Sci. Rev.* 169, 148–172.
- Patton, H., Hubbard, A., Andreassen, K., Winsborrow, M., Stroeven, A.P., 2016. The build-up, configuration, and dynamical sensitivity of the Eurasian ice-sheet complex to Late Weichselian climatic and oceanic forcing. *Quat. Sci. Rev.* 153, 97–121.
- Pedrosa, M., Camerlenghi, A., De Mol, B., Urgeles, R., Rebesco, M., Lucchi, R.G., et al., 2011. Seabed morphology and shallow sedimentary structure of the Storfjorden and Kveithola trough-mouth fans (north west Barents Sea). *Mar. Geol.* 286 (1–4), 65–81.
- Pelle, T., Bondzio, J.H., et al., 2019. Brief communication: PICOP, a new ocean melt parameterization under ice shelves combining PICO and a plume model. *Cryosphere* 13 (3), 1043–1049.
- Peltier, W., 2004. Global glacial isostasy and the surface of the ice-age Earth: the ICE-5G (VM2) model and GRACE. *Annu. Rev. Earth Planet Sci.* 32, 111–149.
- Peltier, W., Argus, D., Drummond, R., 2015. Space geodesy constrains ice age terminal deglaciation: the global ICE-6G_C (VM5a) model. *J. Geophys. Res.: Solid Earth* 120 (1), 450–487.
- Petrini, M., 2017. *Reconstructing with Numerical Ice Sheet Models the Post-LGM Decay of the Eurasian Ice Sheets: Data-Model Comparison and Focus on the Storfjorden (Svalbard) Ice Stream Dynamics History*. Ph.D. thesis. Università degli Studi di Trieste.
- Petrini, M., Colleoni, F., Kirchner, N., Hughes, A.L., Camerlenghi, A., Rebesco, M., Lucchi, R.G., Forte, E., Colucci, R.R., Noormets, R., 2018. Interplay of grounding-line dynamics and sub-shelf melting during retreat of the Bjørnøyrænna Ice Stream. *Sci. Rep.* 8 (1), 7196.
- Peyaud, V., Ritz, C., Krinner, G., 2007. Modelling the Early Weichselian Eurasian Ice Sheets: role of ice shelves and influence of ice-dammed lakes. *Clim. Past* 3 (3), 375–386. <https://doi.org/10.5194/cp-3-375-2007>. <https://www.clim-past.net/3/375/2007/>.
- Pflaumann, U., Sarnthein, M., Chapman, M., d'Abreu, L., Funnell, B., Huels, M., Kiefer, T., Maslin, M., Schulz, H., Swallow, J., et al., 2003. Glacial north Atlantic: sea-surface conditions reconstructed by GLAMAP 2000. *Paleoceanogr. Paleoclimatol.* 18 (3).
- Piasecka, E.D., Winsborrow, M.C., Andreassen, K., Stokes, C.R., 2016. Reconstructing the retreat dynamics of the Bjørnøyrænna Ice Stream based on new 3D seismic data from the central Barents Sea. *Quat. Sci. Rev.* 151, 212–227.
- Pollard, D., DeConto, R., 2012. Description of a hybrid ice sheet-shelf model, and application to Antarctica. *Geosci. Model Dev. (GMD)* 5 (5), 1273.
- Pollard, D., DeConto, R.M., Alley, R.B., 2015. Potential Antarctic Ice Sheet retreat driven by hydrofracturing and ice cliff failure. *Earth Planet Sci. Lett.* 412, 112–121.
- Polyak, L., Forman, S.L., Herlihy, F.A., Ivanov, G., Krinitsky, P., 1997. Late Weichselian deglacial history of the Svyataya (Saint) Anna trough, northern Kara sea, Arctic Russia. *Mar. Geol.* 143 (1–4), 169–188.
- Pritchard, H., Ligtenberg, S., Fricker, H., Vaughan, D., Van den Broeke, M., Padman, L., 2012. Antarctic ice-sheet loss driven by basal melting of ice shelves. *Nature* 484 (7395), 502–505.
- Pritchard, M.S., Bush, A.B., Marshall, S.J., 2008. Neglecting ice-atmosphere interactions underestimates ice sheet melt in millennial-scale deglaciation

- simulations. *Geophys. Res. Lett.* 35 (1).
- Rebesco, M., Domack, E., Zgur, F., Lavoie, C., Leventer, A., Brachfeld, S., Willmott, V., Halverson, G., Truffer, M., Scambos, T., et al., 2014a. Boundary condition of grounding lines prior to collapse, Larsen-B Ice Shelf, Antarctica. *Science* 345 (6202), 1354–1358.
- Rebesco, M., Laberg, J., Pedrosa, M., Camerlenghi, A., Lucchi, R., Zgur, F., Wardell, N., 2014b. Onset and growth of trough-mouth fans on the north-western Barents Sea margin—implications for the evolution of the Barents Sea/Svalbard ice sheet. *Quat. Sci. Rev.* 92, 227–234.
- Reeh, N., 1991. Parameterization of melt rate and surface temperature in the Greenland ice sheet. *Polarforschung* 59 (3), 113–128.
- Reese, R., Albrecht, T., Mengel, M., Asay-Davis, X., Winkelmann, R., 2018. Antarctic Sub-shelf Melt Rates via PICO. *The Cryosphere*.
- Rignot, E., Jacobs, S., Mouginot, J., Scheuchl, B., 2013. Ice-shelf melting around Antarctica. *Science* 341 (6143), 266–270.
- Rignot, E., Mouginot, J., Morlighem, M., Seroussi, H., Scheuchl, B., 2014. Widespread, rapid grounding line retreat of pine Island, Thwaites, Smith, and Kohler glaciers, west Antarctica, from 1992 to 2011. *Geophys. Res. Lett.* 41 (10), 3502–3509.
- Ritz, C., Rommelaere, V., Dumas, C., 2001. Modeling the evolution of Antarctic ice sheet over the last 420,000 years: implications for altitude changes in the Vostok region. *J. Geophys. Res.: Atmospheres* 106 (D23), 31943–31964.
- Sarnthein, M., Pflaumann, U., Weinelt, M., 2003. Past extent of sea ice in the northern North Atlantic inferred from foraminiferal paleotemperature estimates. *Paleoceanography* 18 (2).
- Schmidtko, S., Heywood, K.J., Thompson, A.F., Aoki, S., 2014. Multidecadal warming of Antarctic waters. *Science* 346 (6214), 1227–1231.
- Schoof, C., 2012. Marine ice sheet stability. *J. Fluid Mech.* 698, 62–72.
- Sergienko, O., Macayeal, D.R., 2005. Surface melting on Larsen ice shelf, Antarctica. *Ann. Glaciol.* 40, 215–218.
- Seroussi, H., Nowicki, S., Simon, E., Abe-Ouchi, A., Albrecht, T., Brondex, J., Cornford, S., Dumas, C., Gillet-Chaulet, F., Goelzer, H., et al., 2019. initMIP-Antarctica: an ice sheet model initialization experiment of ISMIP6. *Cryosphere* 13 (5), 1441–1471.
- Shackleton, C.S., Winsborrow, M.C., Andreassen, K., Lucchi, R.G., Bjarnadóttir, L.R., 2019. Ice-margin retreat and grounding-zone dynamics during initial deglaciation of the Storfjordrenna Ice Stream, western Barents Sea. *Boreas*.
- Shapiro, N.M., Ritzwoller, M.H., 2004. Inferring surface heat flux distributions guided by a global seismic model: particular application to Antarctica. *Earth Planet Sci. Lett.* 223 (1–2), 213–224.
- Stokes, C.R., Clark, C.D., 2001. Palaeo-ice streams. *Quat. Sci. Rev.* 20 (13), 1437–1457.
- Stokes, C.R., Tarasov, L., 2010. Ice streaming in the Laurentide Ice Sheet: a first comparison between data-calibrated numerical model output and geological evidence. *Geophys. Res. Lett.* 37 (1).
- Stone, E., Lunt, D., Rutt, I., Hanna, E., 2010. Investigating the sensitivity of numerical model simulations of the modern state of the Greenland ice-sheet and its future response to climate change. *Cryosphere* 4 (3), 397.
- Sundal, A.V., Shepherd, A., Nienow, P., Hanna, E., Palmer, S., Huybrechts, P., 2011. Melt-induced speed-up of Greenland ice sheet offset by efficient subglacial drainage. *Nature* 469 (7331), 521.
- Svendsen, J.I., Alexanderson, H., Astakhov, V.I., Demidov, I., Dowdeswell, J.A., Funder, S., Gataullin, V., Henriksen, M., Hjort, C., Houmark-Nielsen, M., et al., 2004. Late Quaternary ice sheet history of northern Eurasia. *Quat. Sci. Rev.* 23 (11–13), 1229–1271.
- Tarasov, L., Dyke, A.S., Neal, R.M., Peltier, W.R., 2012. A data-calibrated distribution of deglacial chronologies for the North American ice complex from glaciological modeling. *Earth Planet Sci. Lett.* 315, 30–40.
- Tarasov, L., Richard Peltier, W., 2002. Greenland glacial history and local geodynamic consequences. *Geophys. J. Int.* 150 (1), 198–229.
- Tarasov, L., et al. **Eurasian Ice Sheet Evolution**; -. (In prep).
- Vorren, T.O., Hald, M., Lebesbye, E., 1988. Late cenozoic environments in the Barents Sea. *Paleoceanogr. Paleoclimatol.* 3 (5), 601–612.